

Physical Conditions in the Narrow-Line Region of Markarian 3. I. Observational Results

Nicholas R. Collins¹, Steven B. Kraemer¹, D. Michael Crenshaw², Jose Ruiz¹, Rajesh Deo²,
and Frederick C. Bruhweiler¹

ABSTRACT

We use Hubble Space Telescope/Space Telescope Imaging Spectrograph (HST/STIS) longslit low-resolution spectroscopy from 1150 Å to 10,300 Å to study the physical conditions in the narrow-line region (NLR) of the Seyfert 2 galaxy Markarian 3. We find from the He II $\lambda 1640/\lambda 4686$ line ratio and the Balmer decrement that the extinction within Markarian 3 along the line-of-sight to the NLR is best characterized by a Large Magellanic Cloud (LMC) type extinction curve. We observe an extinction gradient increasing from west to east along the STIS slit (at position angle 71° measured east from north) in both line and continuum emission. We infer from this gradient that the host galaxy disk is tilted towards the observer in the east: the line-of-sight to the eastern emission-line cone intersects more dust in the plane of the galaxy than that to the western cone. From emission-line diagnostics we find that the NLR gas is photoionized by the hidden active galactic nucleus (AGN) continuum and that its density decreases with increasing distance from the center. We model the observed continuum as a combination of reddened host galaxy light from an old stellar population, reddened H⁺ and He⁺ recombination continua, and less reddened scattered light from the central engine with spectral index $\alpha=1$ ($L_\nu \propto \nu^{-\alpha}$). The host galaxy to scattered-light ratio is estimated to be 3:1 at 8125 Å in 0".1 × 1".8 aperture. Using a two-component power-law model for the ionizing continuum ($\alpha=2$ for 13.6 eV < E < 0.2 keV and $\alpha=1$ for 0.2 keV < E < 50 keV) we find that the covering factor (normalized for our observation aperture) of the NLR gas is >0.7%. We estimate that the amount of intrinsic non-ionizing UV continuum scattered into our line-of-sight is 0.04%. This is consistent with our estimate of the scattering fraction for broad C IV $\lambda\lambda 1548, 1551$ emission.

¹Institute for Astrophysics and Computational Sciences, Catholic University of America; and NASA Goddard Space Flight Center, Code 681, Greenbelt, MD 20771; collins@stis.gsfc.nasa.gov, stiskraemer@yancey.gsfc.nasa.gov, ruiz@yancey.gsfc.nasa.gov, fredb@iacs.gsfc.nasa.gov

²Department of Physics and Astronomy, Georgia State University, Astronomy Offices, One Park Place South SE, Suite 700, Atlanta, GA 30303; crenshaw@chara.gsu.edu, deo@chara.gsu.edu

Subject headings: galaxies: individual (Markarian 3) — galaxies: Seyfert — line: formation

1. Introduction

Markarian 3 is classified as a Hubble-type SB0 galaxy (Adams 1977) with a Seyfert 2 (Sy 2) active galactic nucleus (AGN) (Weedman & Khachickian 1969). Its spectrum is characterized by narrow forbidden and permitted emission lines and excess UV flux compared to normal galaxies (Weedman 1973). Thompson et al. (1980), Schmidt & Miller (1985), Miller & Goodrich (1990) and Tran (1995a) observed broad permitted lines and AGN continuum emission in its polarized spectrum. These observations are part of the foundation for the “unified” model for active galaxies (Antonucci 1993; Urry & Padovani 1995). In this model the presence or absence of broad permitted-emission lines and a bright, variable AGN continuum in the observed (unpolarized) spectrum depends on the viewing angle to the central engine. The systemic velocity is 4050 km s^{-1} ($z=0.0135$) based on H I 21 cm emission (Tift & Cocke 1988). The distance to Markarian is 53 Mpc if $H_0=75 \text{ km s}^{-1} \text{ Mpc}^{-1}$. At this distance, $1''$ corresponds to 257 pc.

Markarian 3 has been well studied from X-rays to radio wavelengths. Its NLR has a reverse-“S” shape greater than $2''$ in extent (Capetti et al. 1995). In a study of near-UV to far-IR absorption lines, González Delgado, Heckman & Leitherer (2001) found evidence of an old stellar population in the nucleus of Markarian 3. A $2''$ -long radio jet detected in 5-GHz MERLIN observations (Kukula et al. 1993) has a similar shape and orientation to the NLR morphology determined by HST/Faint Object Camera (FOC) narrow-band imaging observations centered on the [O II] λ 3727, [O III] λ 5007, H α , and H γ emission-lines (Capetti et al. 1995). Its hard X-ray spectrum can be modeled as Compton reflection from molecular gas in a torus that obscures the central source of ionizing radiation (Georgantopoulos 1999; Turner et al 1997). However, Georgantopoulos et al. (1999) found a factor of two variation in the X-ray source flux between 4 keV and 20 keV over a 200-day period in RXTE observations. They inferred that a fraction of the intrinsic X-ray continuum penetrates the putative obscuring torus. A comparison of ASCA, GINGA, and BBXRT data revealed that the extended soft X-ray flux ($E<4 \text{ keV}$), which covers the same $\sim 12''$ range as the extended narrow-line-region (ENLR) (Sako et al. 2000), has shown no such variation over ~ 13 years (Iwasawa et al. 1994).

Ruiz et al. (2001) studied the kinematics of the Markarian 3 NLR using [O III] λ 5007 measurements from a STIS/CCD slitless spectrum and from the same longslit data that is presented in this paper. We use the results of their kinematic analysis in this paper. The

extracted spectra from several locations along the longslit show evidence of two kinematic components: one is redshifted and the other is blueshifted in the rest-frame of Markarian 3. These components are interpreted as line-of-sight observations of radially outflowing gas on opposite sides of a NLR bi-cone. Their best-fit kinematic model for a NLR with an angular extent of $2''$ and inner and outer opening half-angles of 15° and 25° , respectively, is radial acceleration from the nucleus to a turnover distance (measured along the bi-cone axis) at ~ 80 pc followed by deceleration to the systemic velocity at ~ 260 pc. The maximum space velocity in the model is 1750 km/s. In this model the bi-cone is tilted towards the observer in the east and away from the observer in the west by 5 degrees. The position angle of the the bi-cone is 70° east of north (Schmitt & Kinney 2000). We note that the host galaxy disk major-axis position angle is 28° and the inclination of the disk is 33° (Schmitt & Kinney 2000). We determine the direction of the host-galaxy tilt in this paper.

In this paper we present an analysis of longslit spectra obtained in each of the HST/STIS low-resolution modes: G140L, G230L, G430L, and G750L. These spectra show fifty emission-lines from ~ 21 ions. The brightest emission-lines have an angular extent of $\sim 3.4''$ or a projected linear extent of 870 pc. In §2 we describe the observations and data reduction. In §3 we describe the emission-line measurement procedure and discuss the extinction corrections. In §4 we present temperature, density and ionization diagnostics. In §5 we show the observed continuum and describe its constituents. We also estimate the covering factor of the NLR gas, and the scattering fraction for the continuum produced by the hidden AGN. Our physical picture of the NLR, including the relative orientation of the host galaxy disk, is presented in §6. We summarize our results in §7. In the forthcoming paper II, we will use these observations and the photoionization model code CLOUDY by Ferland (1988) to constrain the sizes, densities, and spatial distribution of gas clouds in the NLR.

2. Observations and Data Reduction

HST/STIS longslit spectra were obtained on 22 August 2000 in all four low-resolution modes, G140L, G230L, G430L, and G750L providing wavelength coverage from 1150 Å to 10,300 Å. The observations are listed in Table 1. The $52'' \times 0.1''$ slit was used for all spectral modes. This aperture is superposed on the target acquisition image in Figure 1. The slit was oriented to position-angle 71° east of north to match the elongated reverse-“S” shaped feature in the NLR. East is towards the bottom of this figure, and North is towards the left, as indicated by the arrows. The target acquisition image was obtained through the STIS long-pass F28X50LP filter, which spans red to near-IR wavelengths. The bright knots in the image are primarily emission from lines that fall within the wavelength range of the

F28X50LP filter. The brightest lines in the visual and near-IR are [O I] $\lambda\lambda$ 6300, 6363, [N II] $\lambda\lambda$ 6548, 6584, H α λ 6563, [S II] $\lambda\lambda$ 6716, 6731, and [S III] $\lambda\lambda$ 9069, 9532.

The spectra were processed with the CALSTIS IDL software developed by Lindler (1998) for the STIS Instrument Definition Team. This software is used to perform bias and dark subtraction, hot pixel correction, flat-field division, and for the CCD images, cosmic-ray rejection. Hot pixels were identified in STIS dark images and corrected by interpolating in the dispersion direction. Cosmic-ray artifacts were removed in the CCD data by comparing the multiple image readouts obtained within each spectral mode. The multiple readouts obtained in the G140L, G430L, and G750L modes were combined to increase their signal-to-noise ratios. The wavelength scales were corrected for zero-point shifts using hole-in-the-mirror (HITM) lamp calibration exposures made after each science exposure. The two G140L spectra have a relative wavelength offset of 0.15 \AA , or 0.25 pixel. Both spectra were shifted to match a central wavelength of 1418.821 \AA . No such shifts were required for the mode G430L and mode G750L input spectra.

The spectra were processed in “extended-source” mode. In this mode, each column of the output spectral image corresponds to a unique wavelength and each row corresponds to a unique spatial position. This rectification was performed using a bi-linear interpolation algorithm (Lindler 1998). The units of the output spectral image are $\text{ergs s}^{-1} \text{ cm}^{-2} \text{ \AA}^{-1} \text{ cross-dispersion-pixel}^{-1}$. In addition to this rectification, all spectral images were transformed to the same spatial plate scale (1 pixel = $0''.05071$) and alignment as that of spectral mode G430L. This simplifies comparison of the same NLR clouds observed in different spectral modes. The co-alignment among modes in the spatial direction was determined by cross-correlating the slit fiducial marks that are evident in the respective wavelength calibration spectra.

Finally, a background correction was made for each of the spectral images. For modes G230L, G430L, and G750L, the background subtraction algorithm follows that described by Lindler (1998) for point-source extractions. Briefly, two eleven-pixel wide strips are selected a suitable distance away (typically more than 200 pixels, or $10''$) from the center of the NLR spectrum. Each strip is averaged in the spatial direction, then the two average background spectra are in turn averaged together. The resultant background spectrum was smoothed three times: once with a median filter, and again with two different mean filters. This smoothed background spectrum was subtracted from each line of the spectral image.

The background subtraction for mode G140L required more care due to contamination from geo-coronal Ly α λ 1216 and O I λ 1303 emission. The pixels in the averaged, smoothed background spectrum that contain the two geo-coronal lines were replaced with pixels from the averaged, unsmoothed background spectrum. This method minimizes subtraction resid-

uals at the positions of these lines.

We examined the impact of fringing on the CCD/G750L mode spectrum. Fringing in the STIS/CCD G750L mode spectra can reach peak-to-peak amplitude variations of greater than 20% at $\lambda > 9000 \text{ \AA}$ (Proffitt et al. 2002; Malumuth et al. 2003). The fringing is caused by interference among reflected waves in the CCD substrate. We investigated the fringe amplitude of our data using a tungsten lamp flat-field (Plait 2000) and a model flat-field (Malumuth et al. 2003). We concluded that the uncertainty in the data in the wavelength region affected by fringing ($\lambda > 7500 \text{ \AA}$) is dominated by Poisson noise rather than fringing. No correction for fringing was deemed necessary.

We display $1''.8$ sub-image extractions from the co-aligned, background-subtracted spectral images for G140L, G230L, G430L and G750L in Figures 2, 3, 4, and 5, respectively. The overlaid 1-D spectrum is the sum of the spectral image in the cross-dispersion direction. The spatial orientation of each spectral image is West at the top of the figure and East at the bottom of the figure, consistent with Figure 1. We detected over 60 emission lines from ionic species that require ionization potentials up to 100 eV.

3. Emission-Line Measurements

3.1. Integrated Fluxes

We made seven discrete measurements of each emission line in the spatial direction. Individual spectra were extracted by summing array rows in selected bins in the spatial direction. The bin sizes were selected to extract spectral information for individual clouds and to achieve a reasonable signal-to-noise ratio for the the He II $\lambda 1640/\lambda 4686$ measurement which is used to determine the extinction along the line-of-sight to the NLR (see §3.2). The bin sizes range from 0.2-0.3 arcseconds, or 52-77 pc, using the adopted distance scale described in the Introduction. The full spatial range along the slit spanned by the defined bins was also constrained by the spatial extent of the two He II emission lines. Several emission-lines have spatial extents greater than the analyzed $1''.8$ range, but the extinction correction outside this range cannot be determined from the low signal-to-noise He II emission.

The measurement bins are shown in Figure 6. The bins were selected by visually comparing the spatial profile of each emission-line with that of the target acquisition direct image. The arrow on each row of displayed emission lines indicates bin $0''.0$. It contains the kinematic zero-point in the Ruiz et al. (2001) velocity map. This coincides with the position of the hidden-nucleus derived by Kishimoto et al. (2002) from UV-imaging polarimetry data.

The line flux measurement procedure began by removing all lines except the line of interest from the one-dimensional spectral extraction. We executed this removal by interpolating between continuum values adjacent to each unwanted line. We then performed a linear fit to the remaining continuum. We subtracted this fit from the spectrum, then fitted a Gaussian function to the line of interest. The uncertainties in the line fluxes were estimated by making three such measurements for each line, each time interactively selecting different continuum regions. The wavelength range of the continuum regions varied between the full spectral range of the spectral mode of interest (G140L: 611 Å, G230L: 1616 Å, G430L: 2800 Å, and G750L: 5030 Å) and one-third of the the full range. The reported line flux is the average value of the three measurements. The line flux uncertainty is the standard deviation of the three measurements added in quadrature with the uncertainties from Poisson statistics. This uncertainty is dominated by the standard deviation of the three line flux measurements.

In any measurement bin where two kinematic components and/or two different lines are blended together, we used the [O III] $\lambda 5007$ solution for that bin as a template. There were no compelling incidences where three or more components were required to fit the measurements using the selected bins. We assumed that the kinematics of the [O III] $\lambda 5007$ gas matches that of the line of interest. The [O III] $\lambda 5007$ measurements with two components were fitted with six free parameters, or three for each of the two components: the peak flux, the Gaussian standard deviation, and the central wavelength. The Gaussian standard deviations were converted to velocity dispersions. The fitted central wavelengths were used with the rest wavelength to compute the radial velocities of the components. The dispersions were converted to Gaussian standard deviations for the line(s) of interest. These standard deviations were corrected to match the observed line profiles by adding in quadrature the appropriate spectral resolution term from Table 1. The radial velocities were used to derive the wavelength offsets for the line(s) of interest. This procedure leaves only the peak fluxes of the components as free parameters in the Gaussian fits for the line(s) of interest. The lines deblended in this manner were [Ne III] $\lambda 3869$ from H8 $\lambda 3889$, [S II] $\lambda 4074$ from H δ $\lambda 4102$, H γ $\lambda 4340$ from [O III] $\lambda 4363$, [Fe VII] $\lambda 5159$ from [N I] $\lambda 5200$, [Fe VII] $\lambda 5722$ from [N II] $\lambda 5755$, [O I] $\lambda 6300$ from [O I] $\lambda 6363$, and He I $\lambda 7065$ from [Ar III] $\lambda 7136$. For the H α $\lambda 6563$ + [N II] $\lambda\lambda 6548, 6584$ blend we fixed the [N II] $\lambda 6584/\lambda 6548$ flux ratio to 3:1 in addition to the aforementioned constraints. The 3:1 ratio applies to a $\sim 10,000$ K nebulae with density less than 10^5 cm $^{-3}$. This is the critical density required to collisionally de-excite the upper level (1D_2) responsible for the [N II] $\lambda\lambda 6548, 6584$ doublet emission. We used the same procedure to deblend the C IV $\lambda\lambda 1548, 1551$ doublet and the Mg II $\lambda\lambda 2796, 2803$ doublet. For both of these doublets the short-to-long wavelength line-flux ratio constraints are 2:1 for optically thin lines. The spectral resolution is too low to separate the individual components of the remaining blended lines: Si IV $\lambda 1398$ multiplet with the O IV] $\lambda 1402$ multiplet, and

[S II] $\lambda 6716$ with [S II] $\lambda 6731$. Figure 7 shows the fit for the two-component [O III] $\lambda 5007$ line in the central bin. We list flux measurements relative to H β $\lambda 4861$ for forty-six emission lines at seven spatial positions in Table 2. The 1σ uncertainties in the observed flux ratios are listed in parentheses below each measurement.

3.2. Extinction Correction

We corrected the observed flux measurements for both Galactic extinction along the line-of-sight to Markarian 3, and intrinsic extinction caused by dust within Markarian 3. The Galactic color-excess of $E(B-V) = 0.19$ was obtained from the dust map of Schlegel et al. (1998). We used the Savage & Mathis (1979) extinction curve to correct for Galactic extinction.

We used the He II $\lambda 1640/\lambda 4686$ line ratio (Seaton 1978) to determine the extinction within Markarian 3 along the line-of-sight. This ratio has a longer wavelength baseline than the Balmer decrement (H α $\lambda 6563$ /H β $\lambda 4861$) and therefore gives a better estimate of the reddening. It is also insensitive to collisional excitation. The ratio can vary from 5.6 for a low density ($n_e \rightarrow 0 \text{ cm}^{-3}$) 5,000 K plasma to 7.6 for a high density ($n_e \sim 10^6 \text{ cm}^{-3}$) 20,000 K plasma (Seaton 1978). We used a ratio of 7.2. This is appropriate for a 10,000 K nebula with Case B recombination and $n_e < 10^4 \text{ cm}^{-3}$ (Seaton 1978). We calculated the color excess for each measured NLR component using the following screen geometry relation

$$E(B - V) = 2.5 \times \log_{10}(7.2 \times (f_{4686}/f_{1640})) / (X_{1640} - X_{4686}) \quad (1)$$

where f_{4686} and f_{1640} are the Galactic extinction corrected He II line fluxes and X_{1640} and X_{4686} are the normalized extinction values ($X_\lambda \equiv E(\lambda - V) / E(B-V)$) at the wavelengths of the He II lines. The 1σ uncertainties in the color excess values are on the order of the range of color excess values calculated using the theoretical upper and lower limits of the He II $\lambda 1640/\lambda 4686$ line ratio described above.

To determine the best extinction curve for the NLR of Markarian 3, we calculated $E(B-V)$ using several different curves from the literature, applied the different color excess values to the H α $\lambda 6563$ and H β $\lambda 4861$ flux measurements, and compared the resultant Balmer decrement values with theoretical values. The Balmer decrement can vary from 2.74 for a high density ($n_e = 10^6 \text{ cm}^{-3}$) 20,000 K gas to 3.05 for a low density ($n_e \rightarrow 0$) 5,000 K gas assuming Case B recombination (Osterbrock 1989). We also required physically plausible values (typically ≤ 36 [Osterbrock 1989]) for the extinction corrected Ly α $\lambda 1216$ to H β $\lambda 4861$ flux ratios. We used following extinction curves: Galactic (Savage & Mathis 1979), θ^2 Ori B (Bohlin & Savage 1981), the starburst curves of Calzetti et al. (1994) and Calzetti (1997),

SMC-bar (Witt & Gordon 1999), SMC (Hutchings 1982), average LMC (Nandy et al. 1981), average LMC (Koornneef & Code 1981), and separate curves for within and outside of 30 Doradus in the LMC (Fitzpatrick 1985).

The θ^2 Ori B, Galactic, starburst, SMC-bar curves yielded values too low to be physically plausible. The Balmer decrement weighted mean values and their uncertainties are, respectively, 0.44 ± 0.08 , 2.33 ± 0.09 , 2.30 ± 0.13 , 2.36 ± 0.10 , and 2.02 ± 0.11 . The SMC curve (Hutchings 1982) yielded a Balmer decrement weighted mean value of 2.84 ± 0.06 , but the extinction corrected Ly α $\lambda 1216$ values were higher than the theoretical upper limit by factors of up to 2.8. The Nandy et al. (1981) and Fitzpatrick (1985) LMC curves (within and without 30 Doradus) produced weighted mean Balmer decrement values closer to the theoretical limits: 2.53 ± 0.08 , 2.52 ± 0.08 (30 Dor), and 2.35 ± 0.08 (non-30 Dor), respectively. We found that the LMC curve of Koornneef & Code (1981) gave a weighted mean value of the Balmer decrement (2.59 ± 0.07) closest to the theoretical values and yielded physically plausible values for the Ly α $\lambda 1216$ to H β $\lambda 4861$ flux ratios. We used this curve to de-redden the observed fluxes using a screen geometry in this paper. The extinction corrected line fluxes relative to H β $\lambda 4861$ are listed in Table 3. The 1σ line-ratio uncertainties include a component due to the uncertainty in the extinction correction.

The simple grain model of Mathis et al. (1977) for standard Galactic extinction curves attributes the continuous extinction to a size-distribution of various grains, and the 2200 Å bump to smaller (mainly graphite) grains. The empirically derived Koornneef & Code (1981) LMC curve exhibits a less pronounced 2200 Å bump and increases more steeply with decreasing wavelength for $\lambda < 2200$ Å. The steeper rise of the Koornneef & Code (1981) LMC curve is attributed to an overall smaller distribution of dust grains than are required to produce the Galactic, starburst, and SMC-bar extinction curves described in this section. The agreement of the He II $\lambda 1640/\lambda 4686$ ratios and the Balmer decrement values with their theoretical values after applying the Koornneef & Code (1981) LMC curve suggests that the dust grain size distribution in the observed area of the Markarian 3 NLR is smaller than the standard Galactic distribution. Pitman & Clayton (2000) note that many active galaxies have dust extinction characterized by the absence of the 2200 Å feature. The reddening curve is generally similar to that of the narrow-line Sy 1 Arakelian 564 (Crenshaw et al. 2002), but not as steep as that of the SMC (Hutchings 1982).

The color excess is shown as a function of position in the NLR in Figure 8. There is a striking gradient in extinction increasing from west to east. This result might also have been inferred from inspection of the spectral images. Compare the spatial morphology of UV emission lines in Figures 2 and 3 with that of optical lines in Figures 4 and 5. Both redshifted and blueshifted points east of the nucleus are reddened, suggesting that the source

of extinction may be an intervening dust lane or screen between the observer and the NLR along the line-of-sight. The extinction gradient suggests that there is more dust in the screen along the line-of-sight to the eastern side of the NLR bi-cone than that of the western side, as observed along the STIS slit. Elmegreen & Block (1999) noted that dust in an inclined galactic plane can produce a similar extinction gradient in which the side tilted towards the observer is more reddened than the side that is tilted away (see further discussion on the host galaxy orientation in §6). We note that the magnitude of the extinction gradient is steeper when derived using an extinction curve that increases slowly with shorter wavelength in the UV, such as the θ^2 Ori B (Bohlin & Savage 1981) curve. The Hutchings (1982) SMC curve, which increases faster with decreasing wavelength in the UV, produces a shallower extinction gradient than that derived with the LMC Koornneef & Code (1981) curve.

Kraemer et al. (2000) found no clear trend over their measured region ($\pm 3''$, or $\sim \pm 200$ pc for $z=0.0033$ and $H_0=75$ km s $^{-1}$ Mpc $^{-1}$) of the NLR in NGC 4151 (Sy 1.5), although they note that the extinction may increase from the north-east to the southwest over the inner $\pm 1''$ ($\sim \pm 60$ pc). They concluded that the lack of uniformity in extinction over the entire NLR suggests that the reddening is associated with the emission-line knots, rather than an external screen. Note that the orientation of the NGC 4151 NLR is such that all of the north-east side is redshifted and all of the south-west side is blueshifted (Nelson et al. 2000). This is not surprising since the NLR bi-cone axis is tilted further toward our line-of-sight (35° out of the plane of the sky [Evans et al. 1993]) than that in Markarian 3. The host NGC 4151 galaxy is closer to face-on orientation than Markarian 3 with an inclination of 21° such that the eastern side is tilted towards the observer (Kinney et al. 2000).

In NGC 1068 (Sy 2), Kraemer & Crenshaw (2000b) found in general that measurements of blueshifted clouds exhibited greater extinction than redshifted clouds. They inferred that both red and blueshifted components were observed through a foreground dust-screen, and that additional dust may be associated with the individual blueshifted clouds. The orientation of the NGC 1068 NLR is similar to that of Markarian 3, where blue- and redshifted clouds are observed along the same line-of-sight and the bi-cone axis is tilted towards the observer in the north-east by 5° (Crenshaw & Kraemer 2000). The angular extent measured along the the NLR bi-cone axis was $\pm 5''$, or spatial extent ± 360 pc (for $z=0.0038$ and $H_0=75$ km s $^{-1}$ Mpc $^{-1}$). The host galaxy disk is tilted towards the observer in the south by 28° (Kinney et al. 2000). The covering factors of the blueshifted clouds are expected to be small so that those clouds do not eclipse (and further redden) the redshifted clouds; therefore, the dust responsible for the observed extinction gradient in the Markarian 3 NLR is likely a screen outside the NLR.

We note that most of the emission line profiles in the dual-velocity-component mea-

surement bins (+0′50, +0′25, 0′00, and -0′23) in the Markarian 3 STIS spectra show an asymmetry: the observed flux of the blueshifted velocity component is less than the flux of the redshifted component (e.g. Figure 7). This asymmetry is observed for resonance, semi-forbidden, and forbidden lines. We do not see evidence in Figure 8 that the extinction is commensurately greater for the blueshifted components compared to the redshifted components. The extinction corrected redshifted/blueshifted flux ratios are also typically greater than unity. The redshifted components may be brighter simply because they have higher emissivity (i.e., more gas) than the blueshifted components.

We estimated the hydrogen column density along the line-of-sight to the narrow-line region clouds using our derived color excess values and the relation of Shull & van Steenberg (1985): $N_{HI} = 5.2 \times 10^{21} \text{ cm}^{-2} \times E(B-V)$. We found that the column density varies from $0.35 \times 10^{21} \text{ cm}^{-2}$ to $1.8 \times 10^{21} \text{ cm}^{-2}$ corresponding to our range in calculated $E(B-V)$ of 0.07 to 0.36. These values are reasonable for an S0 galaxy viewed at $i=33$ (Tuffs et al. 2004), the inclination of Markarian 3 (Schmitt & Kinney 2000).

4. Emission-Line Diagnostics

4.1. Ionization Diagnostics

We used emission-line ratios to constrain the ionization mechanism in the NLR. Veilleux & Osterbrock (1987) identified line ratios to distinguish between starburst and AGN continua. They used lines that are close in wavelength to diminish the effects of reddening. We plot the logarithm of the ratio $[N \text{ II}] \lambda 6584 / H\alpha \lambda 6563$ against that of $[O \text{ III}] \lambda 5007 / H\beta \lambda 4861$ in Figure 9. The solid line in each figure separates the starburst parameter space from that for AGN (Veilleux & Osterbrock 1987). The dashed line represents the power-law photoionization model with solar abundance of Ferland & Netzer (1983). The dimensionless ionization parameter varies from 10^{-4} in the lower right to $10^{-1.5}$ in the upper left. The ionization parameter is defined as $U = Q(H) / 4\pi r^2 n_e c$, where $Q(H)$ is the number of ionizing photons emitted by the central source per second, r is the distance between the source and the cloud, n_e is the electron density at the inner face of the cloud, and c is the speed of light. If the density is low enough that collisional de-excitation is negligible ($< 10^3 \text{ cm}^{-3}$ for most of the observed emission-lines), emission-line ratios will depend primarily on U (Ferland & Netzer 1983). For example, the $[O \text{ III}] \lambda 5007 / H\beta \lambda 4861$ and the $[O \text{ III}] \lambda 5007 / [O \text{ II}] \lambda 3727$ ratios increase as U increases.

The observations occupy a small region of parameter space that is approximately 0.2 dex higher than the solar-abundance power-law photoionization model of Ferland & Netzer

(1983). That the observations occupy a small locus of parameter space indicates that the same ionization mechanism, AGN photoionization, applies for all the gas measured along the slit. This is consistent with the results of Kraemer & Harrington (1986) and of Sako et al. (2000) for Markarian 3. The difference between the model and the data in the logarithmic ratio corresponds to a factor of (0.2 dex= $10^{0.2}$) 1.6. This may be an indication that the N/O abundance ratio is somewhat higher than solar (for solar abundances see Lambert (1978)). Such an offset is typical of Sy 2 NLR (see Figure 12.1 in Osterbrock (1989)). An enhanced N/O ratio may be an indication of a greater than solar nitrogen abundance combined with a less than solar oxygen abundance. Oxygen may be depleted onto grains in a dusty nebula. We will investigate this possibility in Paper II.

We also examined the line ratios $\log([\text{O I}] \lambda 6300/\text{H}\alpha \lambda 6563)$ versus $\log([\text{O III}] \lambda 5007/\text{H}\beta \lambda 4861)$. This indicator occupies a small region of its AGN photoionization parameter space similar to that of the $[\text{N II}] \lambda 6584/\text{H}\alpha \lambda 6563$ diagnostic. It does not show the same offset from the Ferland & Netzer (1983) photoionization model however, suggesting that the abundance for oxygen is close to solar. This is also true of the plots in Osterbrock (1989).

4.2. The Ionizing Continuum

The He II $\lambda 4686/\text{H}\beta \lambda 4861$ ratio is sensitive to the shape of the ionizing continuum (Kraemer 1985; Kraemer et al. 1994) if the NLR clouds are ionization-bounded. The line ratio is lower with a steep spectrum than with a flat spectrum because there are less He⁺ ionizing photons in the former case. We assumed that neutral hydrogen is the only absorber of photons with energies between 13.6 eV and 54.4 eV, and that He⁺ is the only absorber of photons with energies greater than 54.4 eV. For a power-law spectrum with spectral index α the ratio of the number of hydrogen ionizing photons, $Q(\text{H}^0)$, to the number of He⁺ ionizing photons, $Q(\text{He}^+)$, is

$$R = \frac{Q(\text{H}^0)}{Q(\text{He}^+)} = \frac{N(\text{He})}{N(\text{H})} \frac{I(\text{H}\beta)}{I(4686)} \frac{j(4686)}{j(\text{H}\beta)} \approx \left(\frac{1}{4}\right)^\alpha - 1 \quad (2)$$

where $N(\text{He})/N(\text{H})$ has the assumed solar value of ~ 0.1 , $I(\text{H}\beta)/I(4686)$ is the extinction-corrected measured line ratio, and $j(4686)/j(\text{H}\beta)$ is the ratio of volume emissivities obtained from Osterbrock (1989). We summed the line fluxes measured in all bins for He II $\lambda 4686$ and H β and found a ratio $I(\text{H}\beta)/I(4686)$ of 4.57. This yields $\alpha=1.36$. This agrees with the value of $\alpha=1.4$ we found for NGC 1068 (Sy 2) (Kraemer & Crenshaw 2000b), NGC 5548 (Sy 1.5) (Crenshaw & Kraemer 1999), NGC 3783 (Sy 1) (Kraemer, Crenshaw, & Gabel 2001), and NGC 4151 (Sy 1.5) (Kraemer & Crenshaw 2000a) in the spectral range $13.6 \text{ eV} < E \lesssim 1 \text{ keV}$. However, if there is a preponderance of matter-bounded clouds, the intrinsic continuum could

be steeper.

4.3. Extinction-Corrected Line Ratios vs. Angular Separation from the Kinematic Center

The ionization-parameter sensitive line ratios can be used to probe the electron density as a function of position within the NLR. If n_e is constant throughout the NLR, the ionization parameter and its diagnostic line ratios decrease as r^{-2} in the NLR (see the definition of the ionization parameter, U , in §4.1). If n_e varies with radius, the radial dependence of U (and its diagnostic line ratios) will be modified since $U \propto (1/r)^2 \times (1/n_e)$. Figure 10 shows the extinction corrected flux ratio $[\text{O III}] \lambda 5007 / \text{H}\beta \lambda 4861$ vs. projected position in the NLR along the STIS longslit aperture. A similar plot for the ratio $[\text{O III}] \lambda 5007 / [\text{O II}] \lambda 3727$ is shown in Figure 11. Using the bi-cone geometry of Ruiz et al. (2001) (inner and outer opening angles of 15° and 25° , respectively, and tilted out of the plane of the sky by 5° towards the observer in the east) and of Schmitt & Kinney (1996) (P.A.= 70°) we can determine the radial distances of the NLR clouds in Markarian 3. We use the solar abundance photoionization model of Ferland & Netzer (1983) to convert the line ratios to photoionization parameter values. The electron density is a constant 10^3 cm^{-3} for this model. The ionization parameter values derived from the two different line ratios are shown as functions of radial distance in Figure 12 and Figure 13. We show curves on the figures representing U corresponding to different radial distributions of n_e . For the curve labeled “2.0”, $n_e \propto (1/r)^{2.0}$ (and U is constant with radius), while n_e is constant with radius (and $U \propto (1/r)^2$ for the curve labeled “0.0”. Note that in the former case, the curve is flat because the radial dependence of the electron density cancels the explicit radial dependence of the ionization parameter. The values of U at large radius in both Figures 12 and 13 lie between the two plotted curves of $n_e \propto (1/r)^{2.0}$ and of $n_e = \text{constant}$. This indicates that the electron density in the NLR decreases with radius from the nucleus. The uncertainty in the ionization parameter is large, but the overall trends in both figures suggest that the decrease is slower than $(1/r)^2$. A patchy gas distribution along the slit in the NLR might be responsible for deviations from the curves. Nelson et al. (2000) and Kaiser et al. (2000) observed similar, although smoother, trends in STIS observations of NGC 4151 and concluded that the electron density decreases slower than r^{-2} in its NLR.

However, collisional de-excitation of the O^+ ions could contribute to the higher line ratio close to the nucleus. The critical densities of the upper-levels responsible for the $[\text{O II}] \lambda 3727$ doublet are $1.6 \times 10^4 \text{ cm}^{-3}$ for $^2\text{D}_{3/2}$ and $3.1 \times 10^3 \text{ cm}^{-3}$ for $^2\text{D}_{3/2}$ (Osterbrock 1989). These are, respectively, factors of 44 and 226 less than the critical density ($7.0 \times 10^5 \text{ cm}^{-3}$) for the

upper level (1D_2) responsible for the [O III] $\lambda 5007$ line (Osterbrock 1989). If the electron density near the center of the NLR were greater than the critical densities for the $^2D_{3/2}$ and $^2D_{3/2}$ levels of O^+ and less than the critical density of the 1D_2 of O^{+2} , then the flux of the [O II] $\lambda 3727$ doublet will drop, and the [O III] $\lambda 5007$ /[O II] $\lambda 3727$ ratio will increase. We find from the density and temperature sensitive emission-line ratios described below, however, that the electron densities in the NLR are probably lower than those conducive to collisional de-excitation. In either case, with or without collisional de-excitation, the drop in the ionization parameter sensitive diagnostics with increasing distance from the nucleus indicates a radial dependence on electron density. Photoionization modeling will be employed in Paper II to further investigate the physical conditions that produce these observed gradients.

The line ratio [O III] $\lambda\lambda(5007+4959)/\lambda 4363$ is a sensitive temperature diagnostic for a photoionized gas in the density range $10 \text{ cm}^{-3} < n_e < 10^4 \text{ cm}^{-3}$. The theoretical value of this ratio decreases with increasing temperature. We detect no obvious trend with spatial position for this diagnostic. The scatter in the [O III] ratio corresponds to an uncertainty in the temperature ranging from 12000 K to 17000 K. A similar temperature range is found in the NLR of NGC 4151 (Nelson et al. 2000).

Although the energy required to produce most of the ions observed in the Markarian 3 NLR is less than 65 eV, two ions, Fe^{+6} and Ne^{+4} require energies of 100 eV and 97 eV, respectively. The spatial profiles of emission lines from these species exhibit striking differences from the lower ionization lines at neighboring wavelengths. The flux drops rapidly from the nucleus to the eastern-most detectable component. This is most dramatically illustrated by comparing the [Fe VII] $\lambda 5721$ and $\lambda 6087$ lines with their neighboring lines, [N II] $\lambda 5755$ and He I $\lambda 5876$, in the mode G750L spectrum (Figures 5 and 6). The fact that lines close in wavelength do not show the same spatial morphology suggests that this is not a reddening effect. The flux measurements for the [Fe VII] $\lambda 5721$ line relative to $H\beta$ $\lambda 4861$ are plotted in Figure 14. Figure 15 shows the flux measurements of [Ne V] $\lambda 3426$ relative to $H\beta$ $\lambda 4861$. The asymmetric spatial profile of the emission-lines from these high-ionization potential ionic species suggests that an absorber located between the BLR and the NLR blocks the continuum above ~ 65 eV that would be required to ionize Fe^{+5} and Ne^{+3} in the eastern side of the NLR. Similar effects have been suggested for NGC 4151 (Alexander et al. 1999) and NGC 1068 (Alexander et al. 2000).

5. The Observed Continuum

5.1. Spectral Decomposition of the Continuum

We examined the observed continuum in the same 1''8 region spanned by the bins defined for the emission-line measurements. Since we found a reddening gradient along the STIS slit increasing from west to east from emission-line diagnostics, we surmised that the intrinsic continuum may also be similarly reddened. We made separate continuum extractions for the east and for the west. The western extraction is the sum of the detector rows corresponding to the bins labeled -0''.8, -0''.5, -0''.2, and 0''.0 in Tables 2 and 3. The eastern extraction is the sum of the rows corresponding to bins 0''.3, 0''.5, and 0''.8. For both extractions we exclude those regions containing emission lines in the row sum. After applying a foreground reddening corresponding to $E(B-V)=0.08$ (LMC extinction curve [Koornneef & Code 1981]) to the western extraction, we found that its shape matched that of the eastern extraction. The flux level of the eastern extraction is 1.4 times greater than that of the extinction-transformed western extraction over the entire observed wavelength range. The eastern spectral extraction and the extinction-transformed western extraction are shown with the model components for the eastern extraction in Figures 16-17. Note that the extinction-transformed western extraction is scaled by 1.4 for comparison with the eastern extraction.

We modeled the observed continuum as a combination of host galaxy stellar light, scattered light from the active nucleus, and recombination emission from H^+ and He^{+2} in the NLR. Stellar light solely from an old population has insufficient far-UV (STIS mode G140L) flux to match the observed spectrum. We determined the relative contribution of the stellar-light and scattered AGN-light components to our observed spectrum using the Kinney et al. (1996) spectral templates for normal galaxies and a simple power-law spectrum. We used the Kinney et al. (1996) S0 galaxy template for the normal galaxy component. We assumed that the spectral index of the power-law component in the observed spectral region is $\alpha=1$. The recombination continuum was determined using the recombination-line and continuous-emission calculations described in Osterbrock (1989). The input variables for these calculations were the sums of the extinction corrected $H\beta$ $\lambda 4861$ and He II $\lambda 4686$ measurements from Table 3 in those bins corresponding to eastern (+0''.3 to 0''.8) and western (-0''.8 to 0''.0) extractions. We applied the Galactic extinction (corresponding to $E(B-V)=0.19$ [Schlegel et al. 1998]) in the direction of Markarian 3 to all components of the model spectrum using the Savage & Mathis (1979) extinction curve. We also applied an extinction corresponding to $E(B-V)=0.08$ using the LMC curve (Koornneef & Code 1981) to all components of the model spectrum to match the eastern extraction. We normalized the stellar and power-law components of the model spectrum so that they matched the data at the 8125 Å measurement bin of the eastern extraction. We scaled and added the two components together,

varying the scale factor to determine the ratio of host galaxy to scattered AGN light that best matched the overall shape of our observed continuum. The signal-to-noise is too low to permit matching absorption lines between the data and the galaxy template. The recombination continuum model components were added to the power-law + host galaxy model. A host galaxy to power-law light ratio of 3:1 at 8125 Å yielded a good match to the data, but we found that additional extinction intrinsic to the Markarian 3 host galaxy, was required to give the best fit at all wavelengths. Applying additional extinction corresponding to $E(B-V)=0.20$ with the LMC curve (Koornneef & Code 1981) to the host galaxy component and to the recombination continuum components gave the best fit to the eastern extraction. The reddened model components for the best fit to the eastern extraction are shown with the eastern and western extractions in Figure 16. The sum of the three model components are shown with the data in Figure 17.

The uncertainty in the host galaxy fraction ($f_{galaxy} = L_{galaxy}/(L_{galaxy}+L_{scattered-AGN})$, where L_{galaxy} and $L_{scattered-AGN}$ are the host galaxy and power-law continua, respectively) is shown by the gray shaded area in Figure 17. The galaxy fraction at 8125 Å ranges from 0.65 to 0.85 across this region. We estimated the uncertainty in the host galaxy extinction for a given host galaxy template and host galaxy extinction value for a fixed galaxy fraction at 8125 Å of 0.75. Varying the host galaxy color-excess from ± 0.05 matches the scatter in the smallest error bars at wavelengths longer than 4000 Å. A variation of ± 0.10 matches the scatter in the largest error bars. Variations at these levels have no effect on the model spectrum at wavelengths less than 4000 Å, where the scattered continuum from the hidden AGN dominates.

Our results for continuum decomposition have a lower galaxy fraction than the previous studies of Koski (1978), Malkan & Oke (1983), and Tran (1995a). The wavelength dependence of the galaxy fraction on our continuum model normalized to 0.75 at 8125 Å is shown in Figure 18. We estimated that the host galaxy fraction reaches 0.8 at the longest wavelengths (>9500 Å) in our model and drops to 0.65 near 4500 Å. The fraction drops off sharply towards shorter wavelengths, amounting to only 0.05 at 2600 Å. The fraction gently decreases to 0.02 at far-UV wavelengths. Koski (1978) reported a galaxy fraction at 4861 Å of 0.78. Malkan & Oke (1983) found a galaxy fraction of 0.88 at 5175 Å and Tran (1995a) computed a fraction of 0.88 at 5500 Å. We found galaxy fractions close to 0.60 at 4861 Å and 5171 Å, and 0.70 at 5500 Å. These differences are likely due to differences in aperture size. The previous studies used apertures of width 2"4, 1", and 2"4, respectively, which admit more host galaxy light than the STIS 0"1 wide slit. If the same amount of scattered nuclear continuum light is observed through all apertures, the host galaxy fraction derived from a large aperture observation will be higher than that derived from a small aperture observation.

We found that the total flux of our observed continuum, integrated in wavelength from 1164 Å to 9670 Å, is 2×10^{-12} ergs s^{-1} cm^{-2} . When corrected for Galactic extinction only, this value is 3.5×10^{-12} ergs s^{-1} cm^{-2} . At a distance of 53 Mpc, this total luminosity is 1.1×10^{42} ergs s^{-1} .

The scattered AGN continuum luminosity can be derived from our power-law fit by recalling that the western component has an unreddened power-law shape with $\alpha=1$ and the eastern component is a reddened ($E(B-V)=0.08$) version of the western component and is 1.4 times brighter. When we add these two components together, and integrate from 1164 Å to 9670 Å we find that the luminosity is 5.8×10^{41} ergs s^{-1} . The total luminosity of the unreddened AGN continuum scattered light integrated from 1164 Å to 9670 Å is 7.4×10^{41} ergs s^{-1} .

5.2. The Covering Factor

We estimated the covering factor, C , of the NLR gas using the relationship between $H\beta$ luminosity and ionizing continuum given by Netzer & Laor (1993)

$$L(H\beta) \simeq 7.4 \times 10^{13} \frac{L_1 C}{\alpha} \text{ ergs } s^{-1} \quad (3)$$

where L_1 is the monochromatic luminosity at 1 Ryd in ergs s^{-1} Hz^{-1} and α is the power-law index above 1 Ryd. This equation applies to an optically thick gas under case B recombination conditions. We summed our extinction-corrected $H\beta$ $\lambda 4861$ flux measurements listed in Table 3 then scaled by the distance factor $4\pi D^2$ to find a total $H\beta$ $\lambda 4861$ luminosity of $7.2 \pm 0.4 \times 10^{40}$ ergs s^{-1} . To find the luminosity at 1 Ryd, we assumed that the ionizing continuum has the form of a two component power-law with a break-point at $\nu = (0.2 \text{ keV})/h$, where h is Planck's constant. We used the spectral index of the ionizing continuum derived in §4.3 of $\alpha=1.36$ for the range $(13.6 \text{ eV}/h) < \nu < (0.2 \text{ keV}/h)$. Turner et al. (1997) used the *ASCA* spectrum of Markarian 3 to estimate that the unabsorbed, intrinsic X-ray spectrum has a spectral index $\alpha=1$ over the range $(0.2 \text{ keV}/h) < \nu < (50 \text{ keV}/h)$ and that its integrated flux from 2 keV to 10 keV is $\sim 10^{44}$ ergs s^{-1} . Using this normalization, we found that $L_1 = 5.0 \times 10^{28}$ ergs s^{-1} Hz^{-1} , and the covering factor is $2.7 \pm 0.15\%$. Netzer & Laor (1993) found typical NLR covering factors for samples of Seyfert 1 galaxies and radio-loud quasars to lie between 1% and 4%. We note that the total ionizing continuum luminosity from 13.6 eV to 50 keV using this two-component model is 6.2×10^{44} ergs s^{-1} .

The covering factor value derived from the $H\beta$ $\lambda 4861$ measurement should be a lower limit since our equivalent aperture of size $0''.1 \times 1''.8$ does not sample the total emitted $H\beta$ $\lambda 4861$ flux. From purely geometrical considerations, the maximum possible covering

factor for our adopted hollow bi-cone geometry (with opening half angles of 15° and 25°) is $(\Delta\Omega/4\pi)\times 100\% = 6\%$. At our adopted distance to Markarian 3 the slit width is 26 pc and our $H\beta$ measurement region covers $\sim 30\%$ of the NLR bi-cone. The upper limit to the covering factor constrained by the superposition of the STIS slit on our bi-cone model is $6\% \times 30\% = 2\%$. This is on the order of our photon-counting derivation lower-limit. Based on this analysis the covering factor within the slit is unity given the bi-cone geometry. However, if we have underestimated the value of L_1 , the covering factor may actually be lower (see below).

We estimated the fraction of intrinsic non-ionizing AGN continuum emission scattered into our line-of-sight. We extrapolated our power-law fit of the observed continuum ($\alpha=1$) to $\nu=(13.6 \text{ eV})/h$ and scaled it to the value of L_1 estimated for the ionizing continuum. The inverse of this scale factor, 0.2%, is the scattering fraction.

We compared the scattering fraction of the continuum with that for BLR emission. We detected scattered C IV $\lambda\lambda 1548,1551$ broad-line emission in a large bin ($1''.8$) extraction equivalent to the full spatial range of the seven emission-line measurement bins. These broad-line wings are indicated by the heavy gray line in Figure 2. Other permitted lines in the STIS spectrum may have scattered broad components, but they also have neighboring lines which make such identification difficult. Of the permitted lines observed in the STIS spectrum, C IV $\lambda\lambda 1548,1551$ and Mg II $\lambda\lambda 2796,2803$ are the most isolated. We do not observe scattered broad-line flux from Mg II.

We followed the procedure of §3.1 to measure the fluxes of the various components of the blended C IV $\lambda\lambda 1548,1551$ lines. We assumed that each narrow line consists of two kinematic components: one redshifted and the other blueshifted. We identified the individual narrow line widths and velocities, relative to the systemic velocity, by using the [O III] $\lambda 5007$ line as a template. We fitted the remaining flux above the continuum with a Gaussian function. The scattered broad-line component flux is $1.25 \times 10^{-14} \text{ ergs s}^{-1} \text{ cm}^{-2}$. The broad-line FWHM of 24 \AA corresponds to a velocity dispersion of $\pm 2200 \text{ km/s}$. After correcting for Galactic extinction (Savage & Mathis 1979) (corresponding to $E(B-V)=0.19$, [Schlegel et al. (1998)]) we found a flux of $5.2 \times 10^{-14} \text{ ergs s}^{-1} \text{ cm}^{-2}$. Accounting for the 53 Mpc distance to Markarian 3 the luminosity of the scattered line emission is $1.6 \times 10^{40} \text{ ergs s}^{-1}$. We note that the equivalent width of the broad-line component is $\sim 125 \text{ \AA}$. This is consistent with the measurements of Wu, Boggess & Gull (1983) for Sy 1 galaxies.

We estimated the intrinsic C IV $\lambda\lambda 1548,1551$ luminosity by assuming a fixed ratio of hard X-ray flux to broad-line flux. We scaled the Markarian 3 hard X-ray flux by that ratio determined for Fairall 9, a Sy 1 galaxy with relatively unabsorbed AGN X-ray continuum emission. We obtained the hard X-ray flux, $f_{2-10 \text{ keV}}=2 \times 10^{-11} \text{ ergs s}^{-1} \text{ cm}^{-2}$, from the TAR-

TARUS database. Wu, Boggess & Gull (1983) listed a C IV $\lambda\lambda 1548,1551$ flux of 7.31×10^{-12} ergs $s^{-1} \text{ cm}^{-2}$ for Markarian 3. Scaling our adopted hard X-ray luminosity of 10^{44} ergs s^{-1} for Markarian 3 by the ratio of C IV $\lambda\lambda 1548,1551$ to hard X-ray flux for Fairall 9 yielded an estimated C IV $\lambda\lambda 1548,1551$ luminosity of 3.7×10^{43} ergs s^{-1} for Markarian 3. Dividing our measurement of the scattered line luminosity by this estimated intrinsic luminosity indicates that the line emission scattering fraction is 0.04%. This is a factor of 5 less than our estimate for the continuum scattering fraction.

We can obtain a better agreement between the continuum and line emission scattering fractions if the ionizing continuum has a steeper spectral index for the range $(13.6 \text{ eV/h}) < \nu < (0.2 \text{ keV/h})$. A larger value for L_1 will lower the scattering fraction for the non-ionizing continuum emission. We hold the hard X-ray normalization fixed at 10^{44} ergs s^{-1} with $\alpha=1$. We used an X-ray to optical energy index of $\alpha_{OX}=1.5$ (Turner et al. 1997) to predict the intrinsic luminosity at 2500 Å. This energy index is the modal value of the α_{OX} distribution for the Braccesi BF quasar subsample studied by Wilkes et al. (1994). We used the non-ionizing continuum index of $\alpha=1$ to extrapolate from 2500 Å to 912 Å (13.6 eV). We then found that the spectral index for the range $(13.6 \text{ eV/h}) < \nu < (0.2 \text{ keV/h})$ is $\alpha \sim 2$. This is the same index that Kraemer & Harrington (1986) used to model the Markarian 3 NLR emission lines. The new value of L_1 is 2.78×10^{29} ergs s^{-1} . Now the scattered fraction of continuum emission is 0.04%, which is consistent with the scattered fraction of intrinsic line emission. We note that the new values of spectral index and ionizing luminosity at 1 Ryd yield a covering factor for the NLR gas of $>0.7 \pm 0.04\%$. This value is well below the geometrical upper limit of 2%. The integrated ionizing luminosity from 13.6 eV to 50 keV is now 1.2×10^{45} ergs s^{-1} .

The discrepancy between the spectral index derived from the He II $\lambda 4686/H\beta$ ratio and that derived from extrapolation using the X-ray to optical energy index may indicate that the Markarian 3 NLR contains some combination of matter-bounded and ionization-bounded clouds. The former derivation applies only to ionization-bounded clouds. Additionally, the ionizing continuum might not be well characterized by a simple power law. It may have a “big blue bump” in the EUV (Sun & Malkan (1989); Krolik et al. (1991)). We will investigate these possibilities using detailed photoionization models in Paper II.

6. Orientation of the NLR Bi-Cone With Respect to the Host Galaxy

Schmitt & Kinney (2000) observed an ellipticity ($e=1-b/a$) of 0.159 in a 60 μm image of Markarian 3. This corresponds to an inclination of 33° ($i = \arccos(b/a)$). However, they were unable to determine the orientation of the Markarian 3 galactic disk. Galactic disk

orientation may be determined using rotation curves derived from neutral hydrogen (21 cm) observations, but no such information for Markarian 3 is currently available in the literature.

Schmitt & Kinney (2000) suggest that dust lanes should lie only on the closer side of a galactic disk, as they would be delineated by background bulge light. We searched for dust lanes in an archival HST/WFCPC2/F606W image obtained by Malkan, Gorjian, & Tam (1998) (exposure time is 500 seconds). After cleaning the cosmic-rays on the single archival image, we created an unsharp-masked image of Markarian 3 to enhance high contrast features that are overwhelmed by the bulge light of Markarian 3. The unsharp-masking process requires dividing an image by a median filtered copy of the same image. We used a 31×31 pixels squared ($1''.43 \times 1''.43$) two-dimensional median filter. The unsharp-masked F606W image is shown in Figure 19. The display in Figure 19 is such that emitting-material appears white and obscuring material (i.e., dust lanes) appear black. The horizontal bar corresponds to 1 kpc or $3''.8$. Note the preponderance of concentric dust lanes found between $4''$ and $12''$ north-east of the nucleus, and the lack of such lanes in the south-west. This is consistent with the reddening gradient observed along the STIS slit that increases from west to east as shown in Figure 8. Based on the orientation of the galaxy disk major axis (P.A.= 28° east of north [Schmitt and Kinney 2000]) and using the bulge back-lighting assumption, we would expect such arcs to be oriented perpendicular to the minor axis on the near side of the galaxy, not perpendicular to the major axis as they appear in Figure 19. However, the presence of dust lanes in the east and not in the west and the bulge backlighting hypothesis suggest that the host galaxy disk is tilted towards the observer in the east along the STIS slit (P.A.= 70° [Schmitt and Kinney 1996]).

We used these clues to the host galaxy inclination and the results of our line diagnostic and continuum studies to develop a physical picture of the Markarian 3 NLR. The reddening gradient derived from the He II $\lambda\lambda 1640, 4686$ line emission shown in Figure 8 suggests the presence of a foreground screen between the observer and the NLR, with increasing extinction from west to east. An extinction gradient is supported by the continuum observations as well: the continuum shape of the western extraction matches the eastern extraction only after applying an amount of extinction corresponding to $E(B-V)=0.08$ using the Koornneef & Code (1981) LMC curve. We infer that the foreground screen is dust within the inclined disk of the host galaxy and argue that the plane of the host galaxy is tilted towards us in the east. We adopt the disk inclination of 33° from Schmitt & Kinney (2000). Ruiz et al. (2001) showed that the NLR bi-cone is tilted towards us in the east as well, although at a smaller angle (5°). The eastern bi-cone is more heavily reddened because we view it through the dust within the galactic plane. The western bi-cone is less reddened since it lies above the plane of the galaxy, or at least the line-of-sight intersects less planar dust than that towards the eastern bi-cone. This configuration is consistent with the findings of Elmegreen

& Block (1999). They suggest that the near side of an inclined disk galaxy will be redder than the far side because the light source is behind most of the disk dust.

In addition to reddening in the east, the contrast in the extinction gradient might be enhanced by preferentially scattered blue continuum emission in the west. If the host galaxy disk is tilted away from us in the west, dust within the disk and throughout or behind the NLR might scatter blue continuum emission into our line-of-sight. Kishimoto et al. (2002) found evidence of more scattering (possibly due to dust) in the west than in the east from a polarized-flux color-map (HST/WFPC2 F275W-F342W) of the Markarian 3 NLR.

Figures 20 and 21 are schematic diagrams of our physical picture of the Markarian 3 NLR shown from two different viewing angles. We show the relative orientation of the components, not their relative spatial scales. The host galaxy disk position-angle measured east from north is 28° and its inclination is 33° (Schmitt & Kinney 2000). The host galaxy disk is tilted towards the observer in the east. The bi-cone orientation parameters from Ruiz et al. (2001) are: position-angle (measured east from north) = 72° , outer-edge opening half-angle = 25° , and inclination = 5° out of the plane of the sky towards the observer in the east. These parameters are derived from the [O III] $\lambda 5007$ morphology and kinematics of the inner 2-3 " of the NLR. In Figure 20 the point-of-view is that of the observer such that the plane of the page is parallel to the plane of the sky. North is at the top of the figure and east is to the left. In Figure 21. The vertical line is parallel to the observer's projected line-of-sight. The observer views the system from the top of the figure. We assume from Figure 8 of Ruiz et al. (2001) that most of the NLR gas is confined within the inner (15° [Ruiz et al. 2001] not shown in the figures) and outer half-opening angles of the bi-cones.

Ruiz et al. (2001) found that there were more redshifted points in the East further out in the ENLR than in the West at comparable distances from the nucleus (see their Figure 4). If the motions of the ENLR are governed by the galactic disk rotation, these observations and the inference that the disk is inclined towards the observer in the East would be consistent with a clockwise (north-to-west) disk rotation as viewed by the observer. Kotilainen & Ward (1997) presented color maps of Markarian 3. Their V-R color map shows a red spiral feature extending approximately $\pm 4''.5$ from the nucleus. If this feature has a kinematic origin and if the spiral arms are trailing the rotation of the galaxy, it would support the hypothesis that the galaxy rotation runs clockwise from north to west.

7. Summary

We used HST/STIS low-resolution longslit spectra to study the physical conditions of the Markarian 3 NLR. We found an extinction gradient in the emission-line and continuum flux increasing from west to east along the STIS slit. The extinction is best characterized with an LMC-type Koornneef & Code (1981) curve. We developed a physical picture of the NLR and host galaxy geometry using the extinction gradient, the NLR-gas kinematic model of Ruiz et al. (2001), and the host galaxy inclination of Schmitt & Kinney (2000). We infer that the host galaxy disk is tilted towards us in the east, providing a dustier line-of-sight to the eastern NLR bi-cone than that to the western bi-cone.

Using emission-line diagnostics for the dimensionless ionization parameter (U) we found evidence for a large scale gradient in electron density in the NLR. The density appears to decrease with radius, although slower than $(1/r)^2$. Small scale deviations from the trend indicate that the gas distribution within the NLR may be patchy. Diagnostics for temperature show no trend with position along the STIS slit. The scatter in the diagnostic suggests an uncertainty in temperature ranging from 12,000 K to 17,000 K. Photoionization diagnostics are consistent with AGN power-law ionizing radiation and show no evidence for a starburst in Markarian 3. We found evidence that the NLR nitrogen to oxygen abundance ratio is a factor of 1.6 above the solar value.

We decomposed the observed continuum as S0 host galaxy stellar light, scattered AGN power-law continuum ($\alpha=1$), and recombination continua from H^+ and He^{+2} . The ratio of host galaxy continuum to scattered power-law continuum is 3:1 at 8125 Å in our aperture. We derived the ionizing continuum ($E \geq 13.6$ eV) as a two-step power law with a breakpoint at 0.2 keV. We used the Turner et al. (1997) estimate of the unabsorbed X-ray spectrum above the breakpoint, where $\alpha=1$ and the 2-10 keV integrated luminosity is 10^{44} ergs s^{-1} . We found $\alpha=2$ for the spectral range 13.6 eV $< E < 0.2$ keV. When we extrapolated from the ionizing continuum to lower energies ($E < 13.6$ eV) and compared the result with the scattered-AGN component of our observed continuum fit we found that the observed scattered-AGN continuum in the UV is 0.04% of the intrinsic AGN continuum. This is consistent with our estimate for the percentage of intrinsic C IV $\lambda\lambda 1548, 1551$ line emission scattered into our line-of-sight. Given our adopted bi-cone geometry, the STIS aperture through which we observed the NLR ($52'' \times 0''.1$), and the ionizing continuum slope $\alpha=2$ at 13.6 eV, the covering factor of the NLR gas is $0.7\% < C < 2\%$.

In Paper II we will use the physical parameters derived from the emission line diagnostics and the inferred ionizing continuum as input to the photoionization model code CLOUDY (Ferland 1988) to confirm our physical picture of the NLR. These models will put tighter constraints on sizes, densities, and spatial distribution of gas clouds in the NLR.

We thank Don Lindler for advice and assistance on using the CALSTIS data calibration pipeline. We are grateful to Charles Bowers and Kazunori Ishibashi for offering valuable insight to co-aligning the STIS spectral images. We thank Eliot Malumuth and Philip Plait for help investigating the fringing in STIS mode G750L. Thanks also to Gary Bower for helpful discussions regarding the host galaxy orientation.

This research has made use of the NASA/IPAC Extra-galactic Database operated by the Jet Propulsion Laboratory, and NASA’s Astrophysics Data System Bibliographic Services. We also made use of the TARTARUS database, which is supported by Jane Turner and Kirpal Nandra under NASA grants NAG5-7385 and NAG5-7067.

Some of the data presented in this paper were obtained from the Multimission Archive at the Space Telescope Science Institute (MAST). STScI is operated by the Association of Universities for Research in Astronomy, Inc., under NASA contract NAS5-26555. Support for MAST for non-HST data is provided by the NASA Office of Space Science via grant NAG5-7584 and by other grants and contracts.

We acknowledge the financial support of NAG5-4103 and NAG5-13109.

REFERENCES

- Adams, T.F. 1977, *ApJS*, 33, 19
- Alexander, T., Sturm, E., Lutz, D., Sternberg, A., Netzer, H., & Genzel, R. 1999, *ApJ*, 512, 204
- Alexander, T., Lutz, D., Sturm, E., Genzel, R., Sternberg, A., & Netzer, H. 1999, *ApJ*, 536, 710
- Antonucci, R.R.J. 1993, *ARA&A*, 31, 473
- Bohlin, R.C. & Savage, B.D. 1981, *ApJ*, 249, 109
- Calzetti, D., Kinney, A.L. & Storchi-Bergmann, T. 1994, *ApJ*, 429, 582
- Calzetti, D. 1997, in *AIP Conf. Ser. 408, The Ultraviolet Universe at Low and High Redshift*, ed. W.H. Waller, M.N. Fanelli, J.E. Hollis, & A.C. Danks (Woodbury: AIP), 403
- Capetti, A., Macchetto, R., Axon, D.J., Sparks, W.B. & Boksenberg, A. 1995, *ApJ*, 448, 600
- Crenshaw, D.M. & Kraemer, S.B. 1999, *ApJ*, 521, 572

- Crenshaw, D.M. & Kraemer, S.B. 2000, ApJ, 532, 101L
- Crenshaw, D.M. et al. 2002, ApJ, 566, 187
- Elmegreen, B.G. & Block, D.L. 1999, MNRAS, 303, 133
- Evans, I.N., Tsvetanov, Z., Kriss, G.A., Ford, H.C., Caganoff, S. & Koratkar, A.P. 1993, ApJ, 417, 82
- Ferland, G.J. & Netzer, H. 1983, ApJ, 264, 105
- Ferland, G.J. 1988, CLOUDY 67.00 (OSU Astronomy Dept.: Internal Report 87-001)
- Fitzpatrick, E.L. 1985, ApJ, 299, 219
- Georgantopoulos, I., Papadakis, I., Warwick, R.S., Smith, D.A., Stewart, G.C. & Griffiths, R.G. 1999, MNRAS, 307, 815
- Gonzalez Delgado, R.M., Heckman, T. & Leitherer, C. 2001, ApJ, 546, 845
- Hutchings, J.B. 1982, ApJ, 255, 70
- Iwasawa, K., Yaqoob, T., Awaki, H. & Ogasaka, Y. 1994, PASJ, 46, 167L
- Kaiser, M.E. et al. 2000, ApJ, 528, 260
- Kinney, A.L., Calzetti, D., Bohlin, R.C., McQuade, K., Storchi-Bergmann, T. & Schmitt, H.R. 1996, ApJ, 467, 38
- Kinney, A.L., Schmitt, H.R., Clarke, C.J., Pringle, J.E., Ulvestad, J.S. & Antonucci, R.R.J. 2000, ApJ, 537, 152
- Kishimoto, M., Kay, L.E., Antonucci, R., Hurt, T.W., Cohen, R.D. & Krolik, J.H. 2002, ApJ, 565, 155
- Koornneef, J. & Code, A.D. 1981, ApJ, 247, 860
- Koski, A.T. 1978, ApJ, 223, 56
- Kotilainen, J.K. & Ward, M.J. 1997, A&A, 121, 77
- Kraemer, S.B. 1985, PhD. thesis.
- Kraemer, S.B. & Harrington, J.P. 1986, ApJ, 307, 478
- Kraemer, S.B., Wu, C.C., Crenshaw, D.M., & Harrington, J.P. 1994, ApJ, 435, 171

- Kraemer, S.B., Crenshaw, D.M., Hutchings, J.B., Gull, T.R., Kaiser, M.E., Nelson, C.H. & Weistrop, D. 2000, *ApJ*, 531, 278
- Kraemer, S.B. & Crenshaw, D.M. 2000, *ApJ*, 531, 278
- Kraemer, S.B. & Crenshaw, D.M. 2000, *ApJ*, 544, 763
- Kraemer, S.B., Crenshaw, D.M., & Gabel, J.R. 2001, *ApJ*, 557, 30
- Krolik, J.H., Horne, K., Kallman, T.A., Malkan, M.A., Edelson, R.A., & Kriss, G.A., *ApJ*371, 541
- Kukula, M.J., Ghosh, T., Pedlar, A., Schilizzi, R.T., Miley, G.K., de Bruyn, A.G. & Saikia, D.J. 1993, *MNRAS*, 264, 893
- Lambert, D.L. 1978, *MNRAS*, 182, 249
- Lindler, D. 1998, *CALSTIS Reference Guide (CALSTIS Version 5.1) (Greenbelt, MD:GSFC)*
- Malkan, M.A. & Oke, J.B. 1983, *ApJ*, 265, 92
- Malkan, M.A., Gorjian, V., & Tam, R. 1998, *ApJS*, 117, 25
- Malumuth, E.M., Hill, R.S., Gull, T., Woodgate, B.E., Bowers, C.W., Kimble, R.A., Lindler, D., Plait, P. & Blouke, M. 2003, *PASP*, 115, 218
- Mathis, J.S., Ruml, W., & Nordsieck, K.H 1977, *ApJ*, 217, 425
- Miller, J.S. & Goodrich, R.W. 1990, *ApJ*, 355, 456
- Nandy, K., Morgan, D.H., Willis, A.J., Wilson, R. & Gondhalekar, P.M. 1981, *ApJ*, 196, 955
- Nelson, C.H., Weistrop, D., Hutchings, J.,B., Crenshaw, D.M., Gul, T.R., Kaiser, M.E., Kraemer, S.B., & Lindler, D. 2000, *ApJ*, 531, 257
- Netzer, H. & Laor, A. 1993, *ApJ*, 404, 51L
- Osterbrock, D.E. 1989, *Astrophysics of Gaseous Nebulae and Active Galactic Nuclei (University Science Books: Mill Valley)*
- Pitman, K.M. & Clayton, G.C. 2000, *PASP*, 112, 537
- Plait, P.C. 2000, private communication.
- Proffitt, C. et al. 2002 "STIS Instrument Handbook", Version 6.0, (Baltimore: STScI)

- Ruiz, J.R., Crenshaw, D.M., Kraemer, S.B., Bower, G.A., Gull, T.R., Hutchings, J.B., Kaiser, M.E. & Weistrop, D. 2001, *AJ*, 122, 2961
- Sako, M., Kahn, S.M., Paerels, F. & Liedahl, A. 2000, *ApJ*, 543, 115
- Savage, B.D. & Mathis, J.S. 1979, *ARA&A*, 17, 73
- Schlegel, D.J., Finkbeiner, D.P. & Davis, M. 1998, *ApJ*, 500, 525
- Schmidt, G.D. & Miller, J.S. 1985, *ApJ*, 290, 517
- Schmitt, H.R., & Kinney, A.L. 1996, *ApJ*, 463, 498
- Schmitt, H.R., & Kinney, A.L. 2000, *ApJS*, 128, 479
- Seaton, M.J. 1978, *MNRAS*, 185, 5P
- Sun, W.H. & Malkan, M.A. 1989, *ApJ*, 346, 68
- Shull, J.M. & van Steenberg, M.E. 1985, *ApJ*, 298, 268
- Tifft, W.G. & Cocke, W.J. 1988, *ApJS*, 67, 1
- Thompson, I., Landstreet, J.D., Stockman, H.S., Angel, J.R.P. & Beaver, E.A. 1980, *MNRAS*, 192, 53
- Turner, J., George, I.M., Nandra, K. & Mushotzky, R.F. 1997, *ApJ*, 488, 164
- Tran, H.D. 1995, *ApJ*, 440, 565
- Tuffs, R.J., Popescu, C.C., Völk, H.J., Kylafis, N.D., & Dopita, M.A. 2004, *A&A*, 419, 821
- Urry, C.M. & Padovani, P. 1995, *PASP*, 107, 803
- Veilleux, S., & Osterbrock, D.E. 1987, *ApJS*, 68, 295
- Weedman, D.W. & Khachikian, E.Ye. 1969, *Astrofizika*, 5, 113
- Weedman, D.W. 1973, *ApJ*, 183, 29
- Wilkes, B.J., Tananbaum, H., Worrall, D.M, Avni, Y., Oey, M.S., Flanagan, J. 1994, *ApJS*, 92, 53
- Witt, A.N. & Gordon, K.D. 2000, *ApJ*, 528, 799
- Wu, C.C, Boggess, A. & Gull, T.R. 1983, *ApJ*, 266, 28

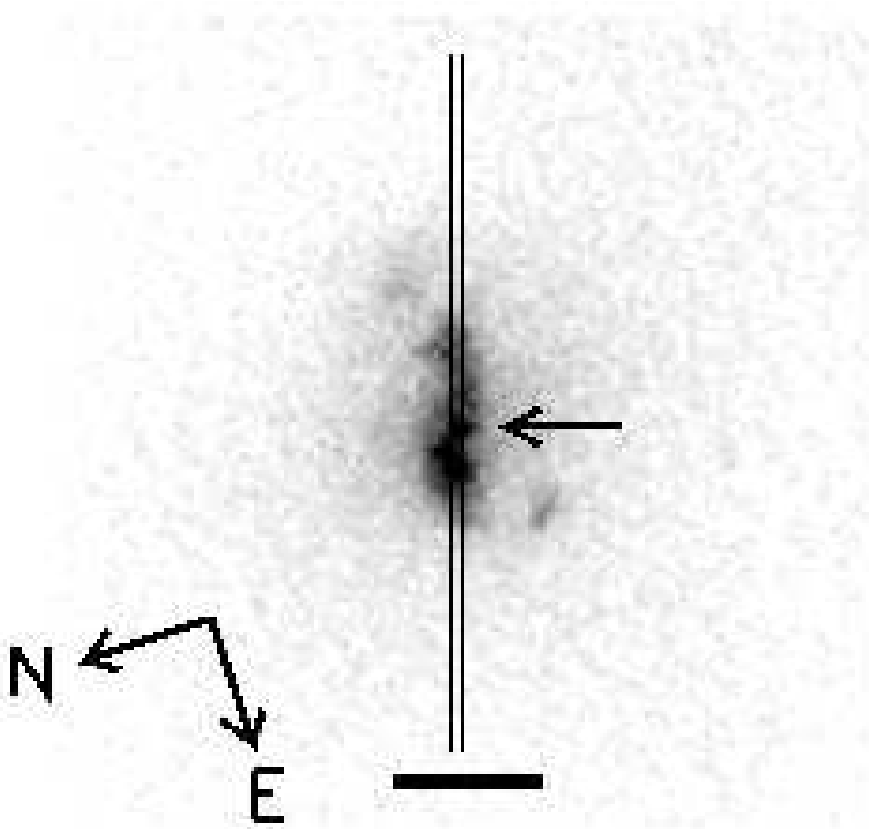


Fig. 1.— STIS target acquisition image obtained through the F28X50LP filter with $52'' \times 0''.1$ slit superposed. The horizontal bar drawn below the NLR is $1''$ or 257 pc in length. The slit is oriented 71° east of north. East is towards the bottom of the figure and North is towards the left. The arrow indicates the NLR kinematic center derived by Ruiz et al. (2001) and the position of the putative hidden nucleus identified by Kishimoto et al. (2002).

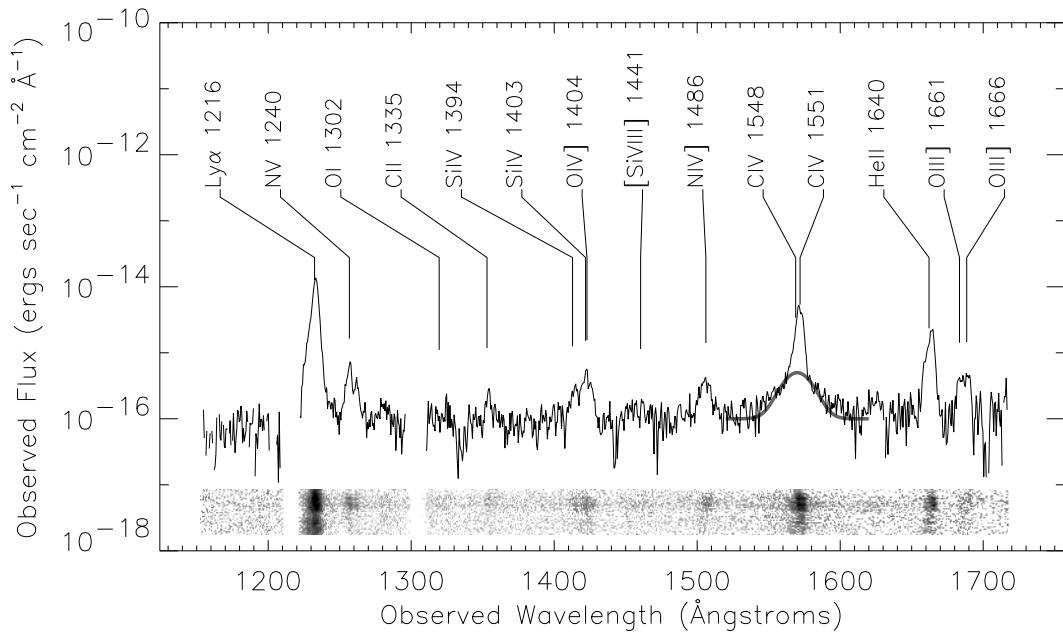


Fig. 2.— 1"8 extraction from G140L spectral image. The heavy gray line at C IV $\lambda\lambda 1548, 1551$ shows the fit to the broad-line flux scattered into our line-of-sight that is discussed in §5.2. The 1"8 spectral image extraction is displayed at the bottom of the panel.

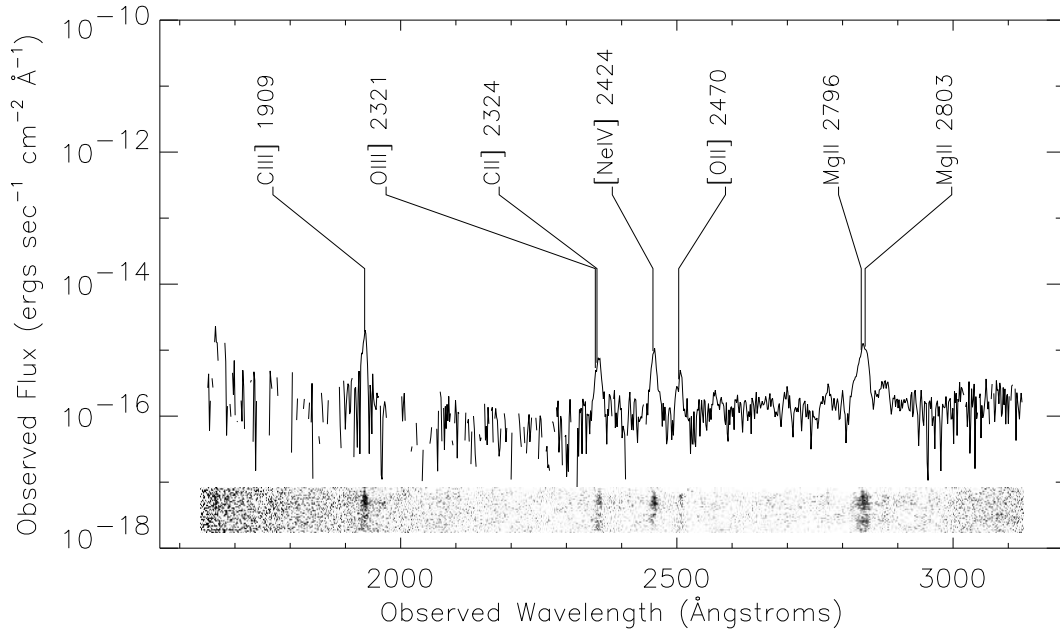


Fig. 3.— 1''8 extraction from G230L spectral image.

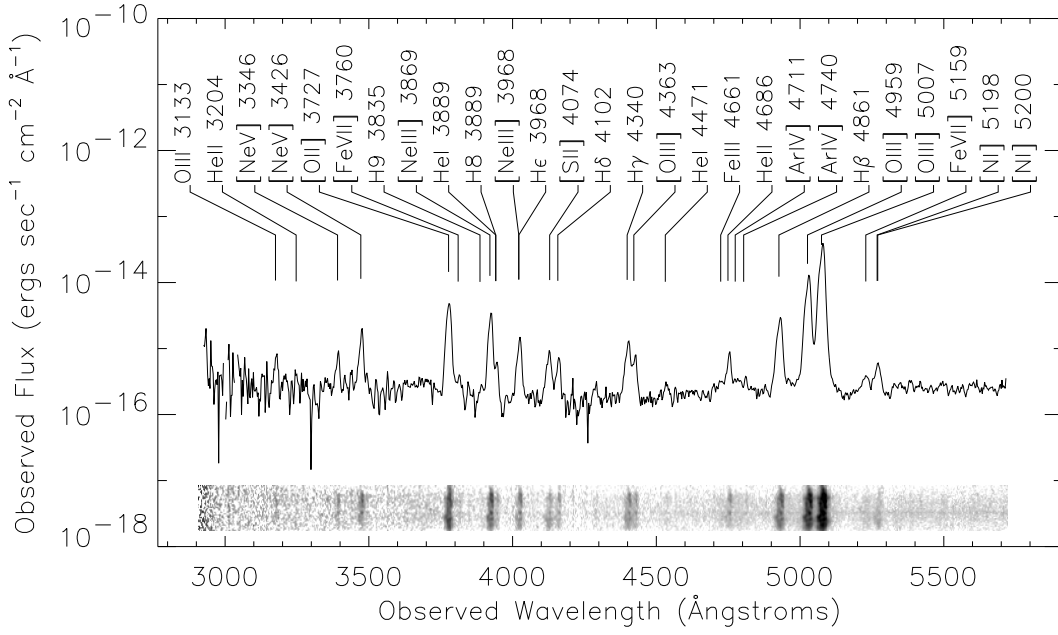


Fig. 4.— $1''8$ extraction from G430L spectral image.

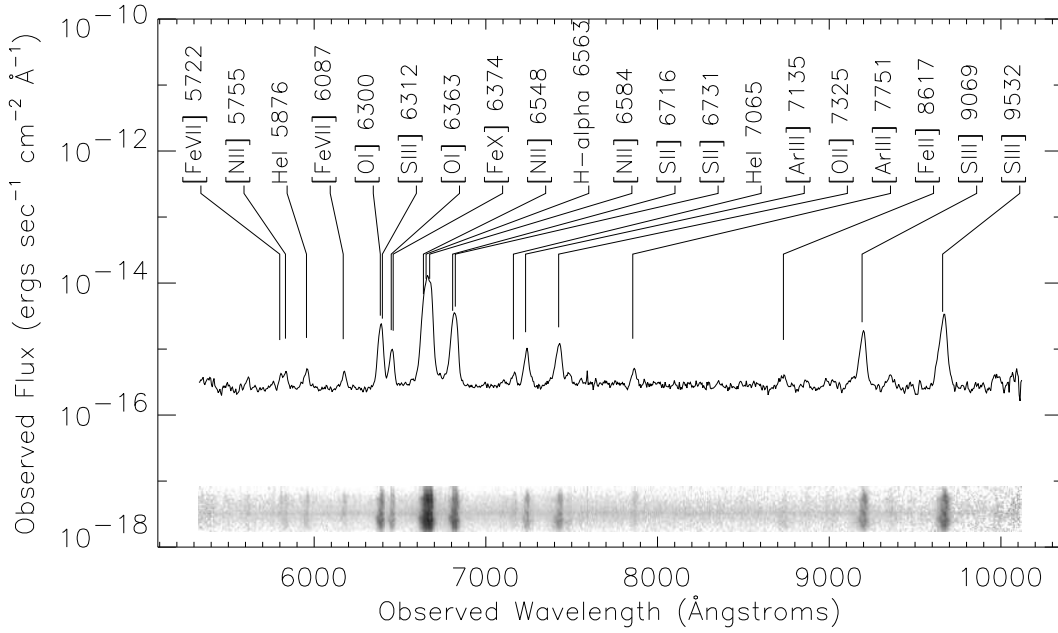


Fig. 5.— $1''8$ extraction from G750L spectral image.

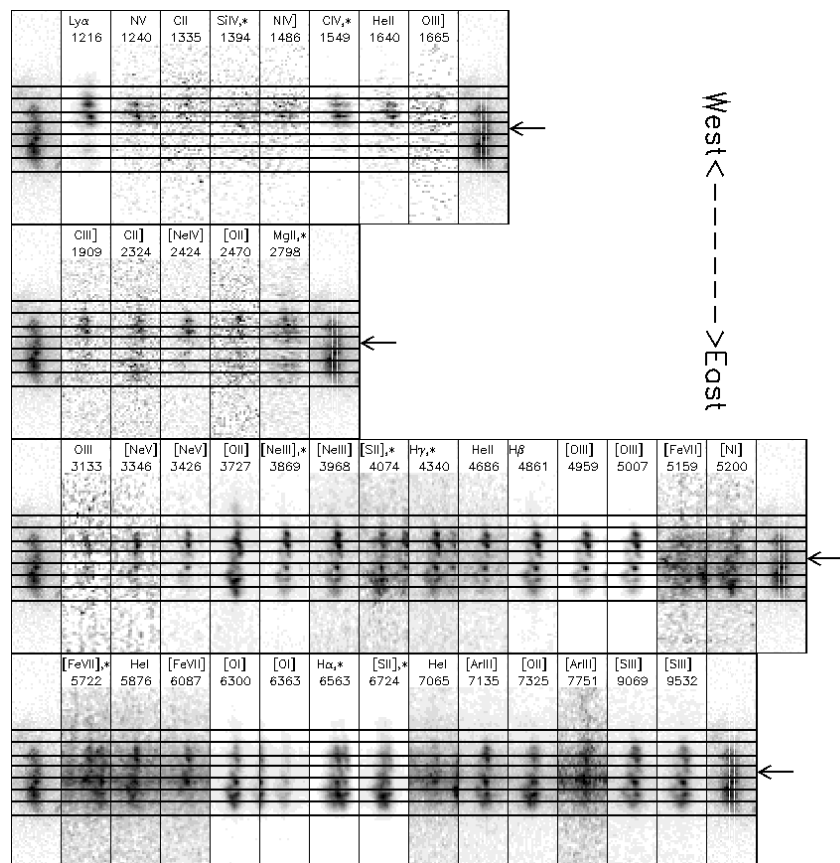


Fig. 6.— Measurement bin diagram shown for 50 emission lines. The spatial orientation is west at the top and east at the bottom. The spatial range from the bottom of the eastern-most bin to the top of the western-most bin is $1''.8$. The spectral range shown for each line is 15 \AA for mode G140L (top row), 40 \AA for mode G230L (second row), 68 \AA for mode G430L (third row), and 123 \AA for mode G750L (bottom row) The target acquisition image (see Figure 1) is duplicated at the ends of each row for reference. At the right end of each row, the $52'' \times 0''.1$ slit boundaries are drawn on the target acquisition image. The asterisks next to some of the line labels indicate that more than one emission line is present in the box. The arrow indicates the bin defined as $0''.0$ in this paper.

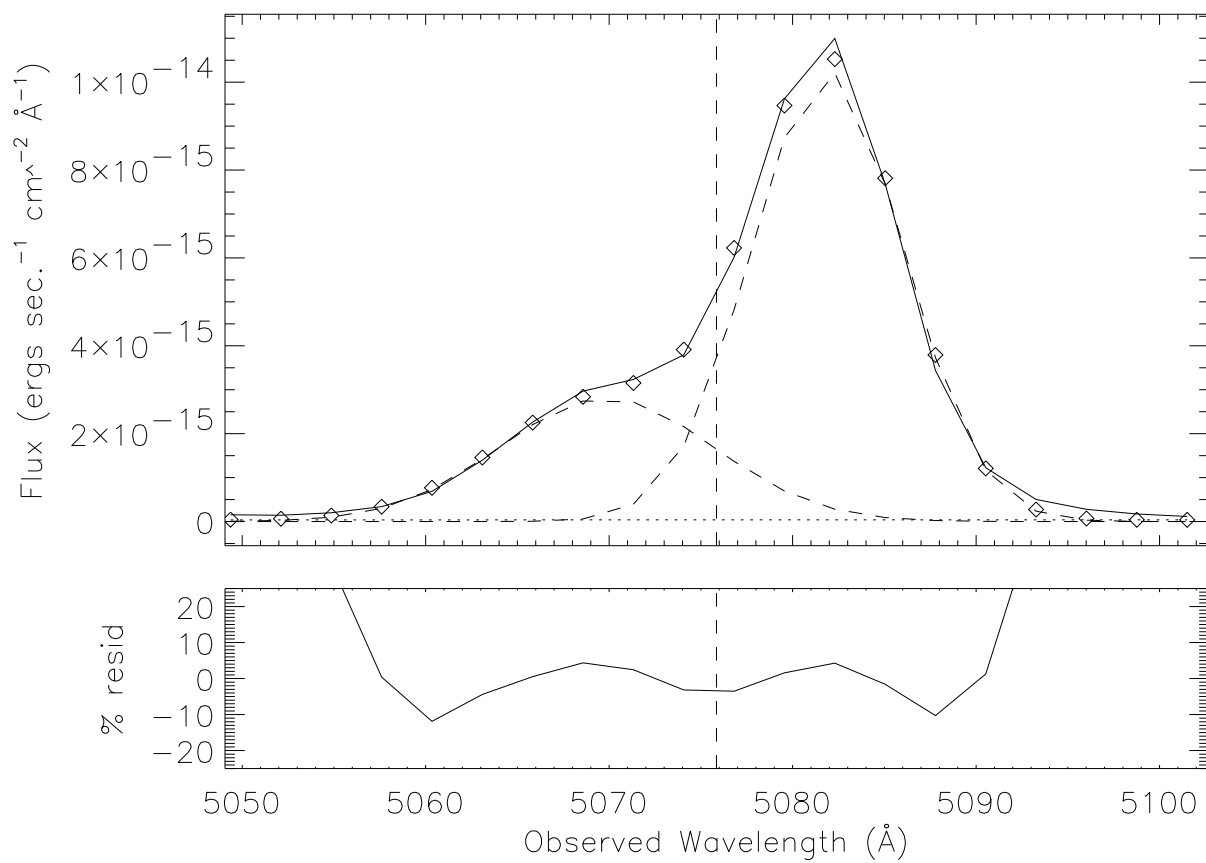


Fig. 7.— Two component Gaussian fit to the [O III] $\lambda 5007$ line in the central bin (position = 0''0). The dashed vertical line indicates the wavelength of [O III] $\lambda 5007$ at the systemic velocity of Markarian 3. The dotted line near the bottom of the emission-line shows the fit to the continuum. The dashed lines show the fits to the two emission-line components. The diamonds show the sum of the emission-line and continuum fits.

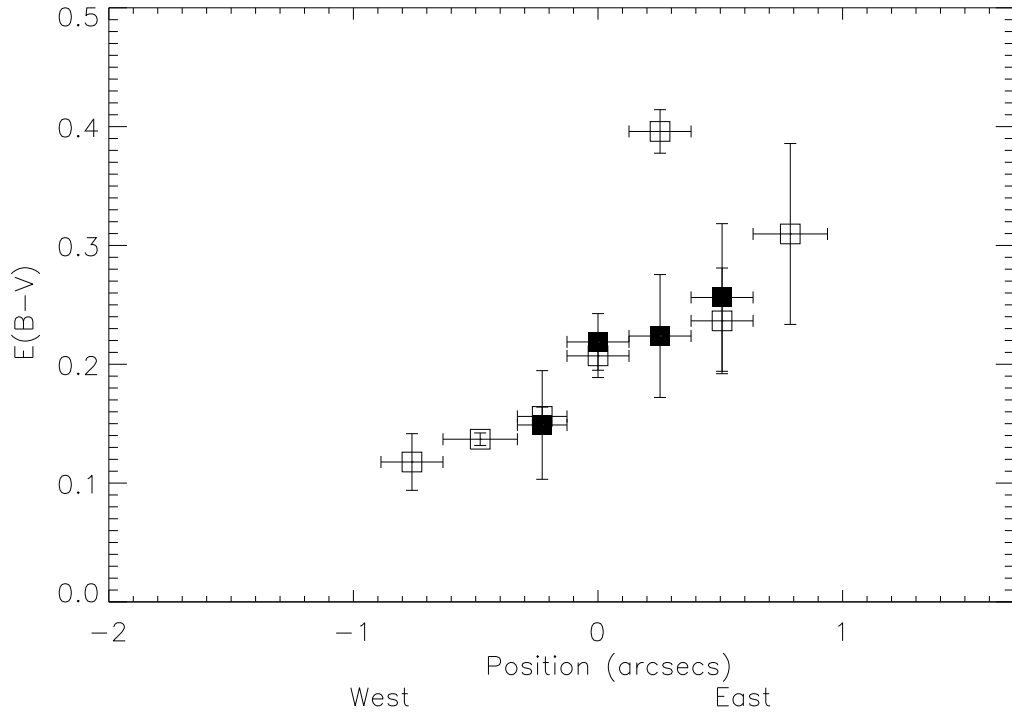


Fig. 8.— $E(B-V)$ color excess as a function of angular separation from the nucleus along the slit. Vertical bars show the uncertainty in $E(B-V)$, and horizontal bars show the angular size of the measured bin. Open squares represent redshifted components and filled squares represent blueshifted components. There is a clear extinction gradient increasing from west to east in the NLR. The zero-point of the position axis for Figures 8-15 is the kinematic center determined by Ruiz et al. (2001).

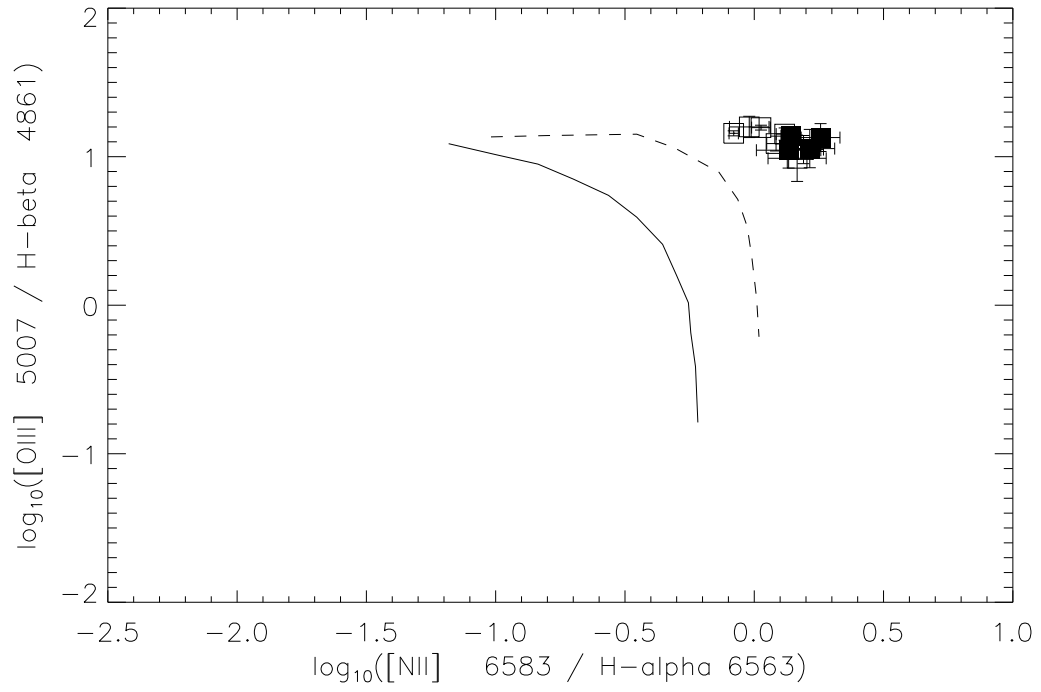


Fig. 9.— Diagnostic ratio plot to test the nature of the ionizing continuum. The solid line separates starbursts from AGN. The dashed line is the power-law photoionization model for solar abundance of Ferland & Netzer (1983).

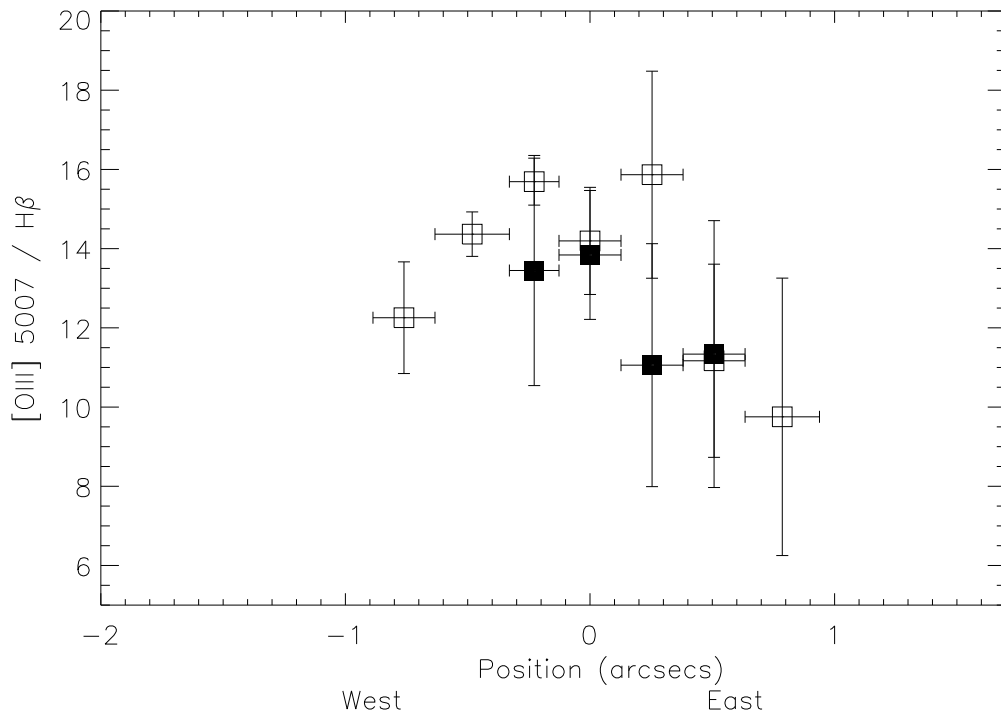


Fig. 10.— The ionization parameter sensitive line ratio $[O III] \lambda 5007 / H\beta \lambda 4861$ vs. angular separation from the nucleus along the slit. Open squares represent redshifted components and filled squares represent blueshifted components. Generally, the ratio decreases with distance from the nucleus for both redshifted and blueshifted components.

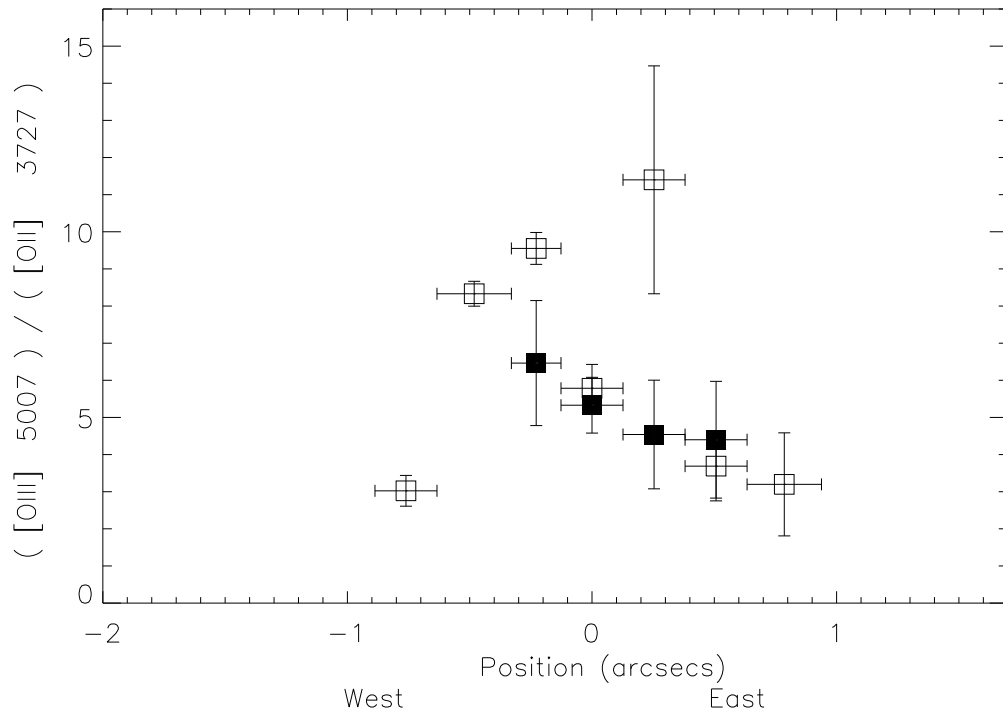


Fig. 11.— The ionization parameter sensitive line ratio $[\text{O III}] \lambda 5007 / [\text{O II}] \lambda 3727$ vs. angular separation from the nucleus along the slit. Open squares represent redshifted components and filled squares represent blueshifted components. The ratio decreases with distance from the nucleus for both redshifted and blueshifted components.

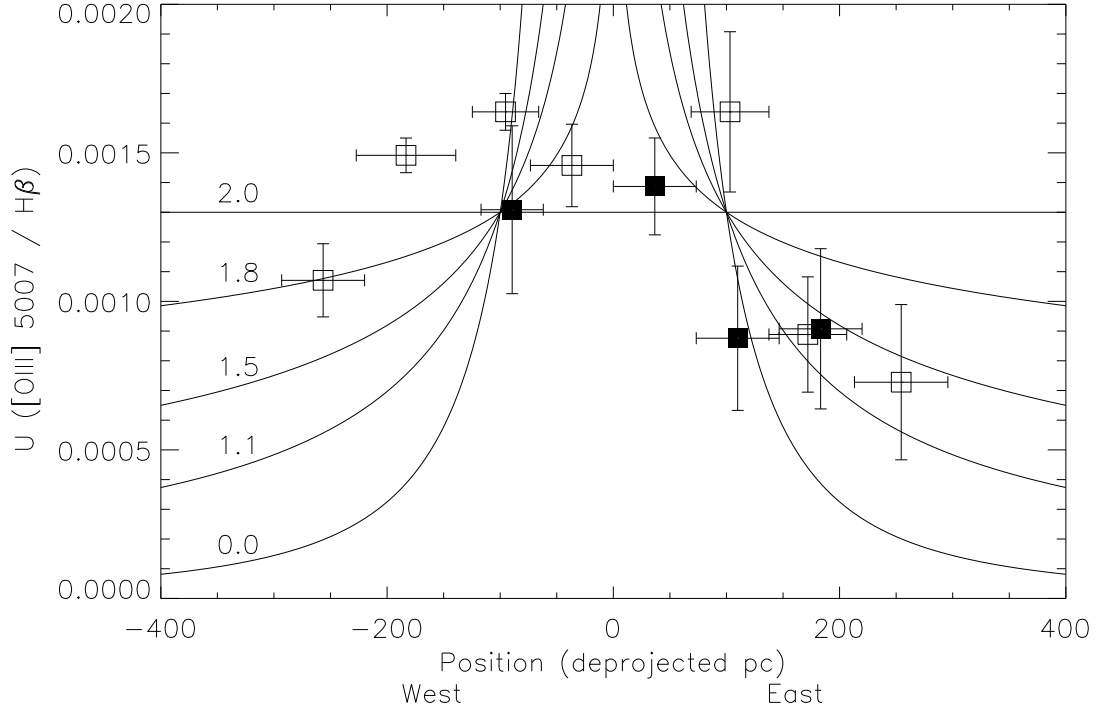


Fig. 12.— The ionization parameter sensitive line ratio $[\text{O III}] \lambda 5007 / \text{H}\beta \lambda 4861$ vs. radial distance from the nucleus towards the east and west along the slit. Open squares represent redshifted components and filled squares represent blueshifted components. The curves represent theoretical ratios for different radial dependencies on electron density. The label above each curve refers to the exponential dependence on radius (for example, the curve labeled 2.0 represents a line ratio for which $n_e \propto (1/r)^{2.0}$). All curves are normalized to a ratio of 0.0013 at a radial distance of 100 pc west.

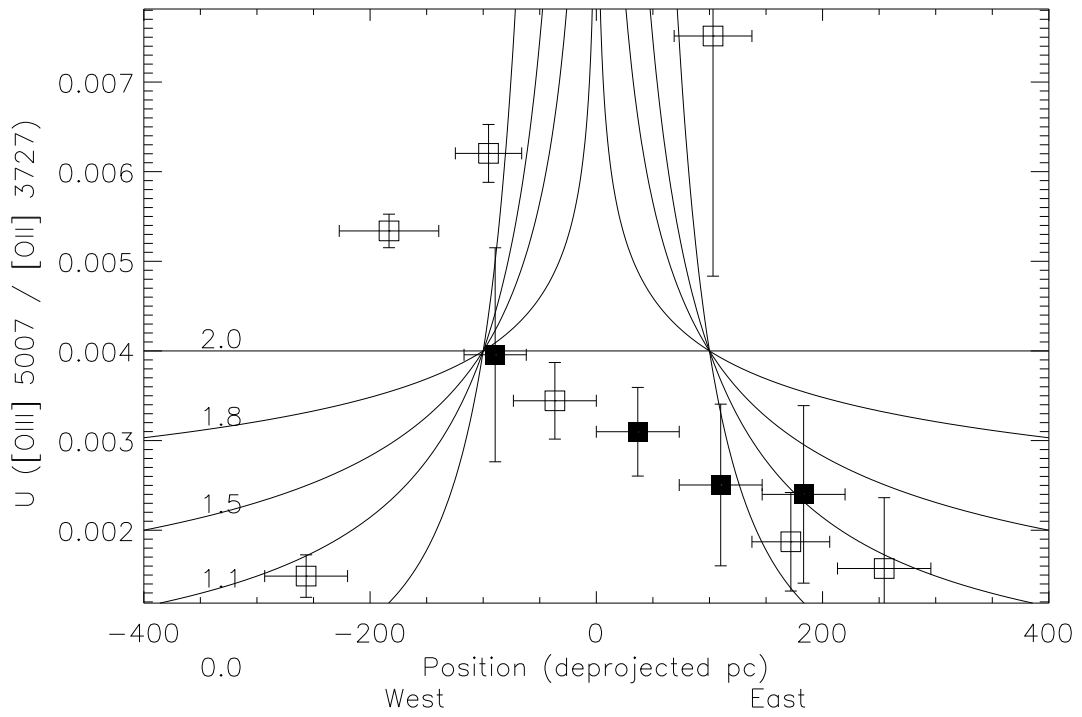


Fig. 13.— The ionization parameter sensitive line ratio $[\text{O III}] \lambda 5007 / [\text{O II}] \lambda 3727$ vs. angular radial distance from the nucleus towards the east and west along the slit. Symbols and curves are the same as those described in Figure 12. All curves are normalized to a ratio of 0.004 at a radial distance of 100 pc west.

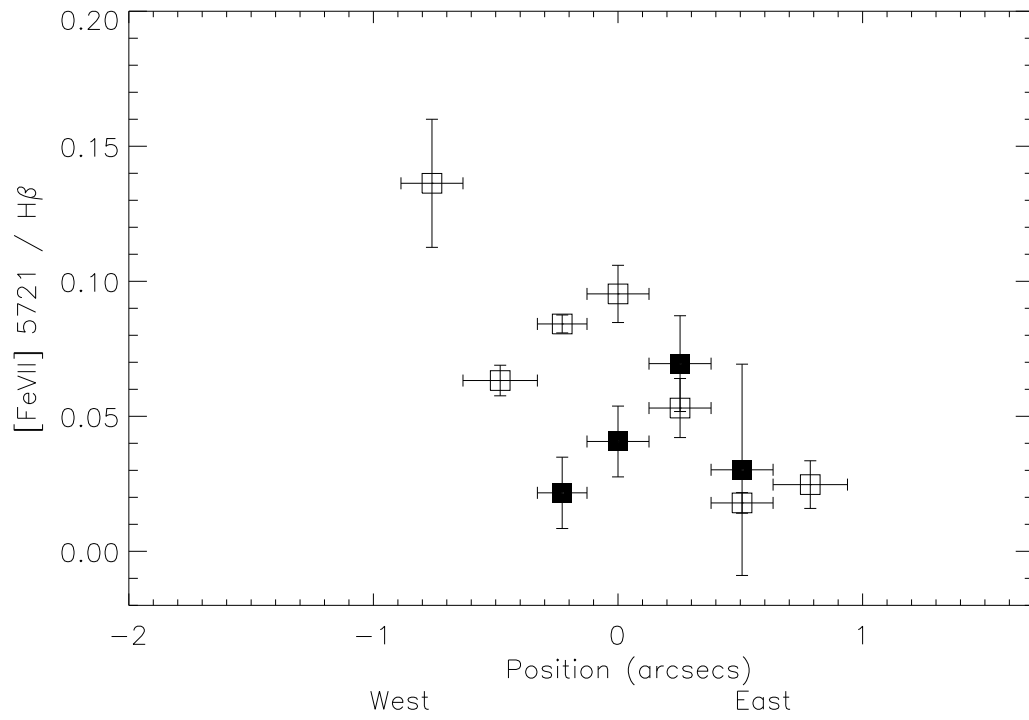


Fig. 14.— [Fe VII] $\lambda 5721$ /H β $\lambda 4861$ plotted as a function of angular separation from the nucleus along the slit. Note the step drop in the ratio to the east.

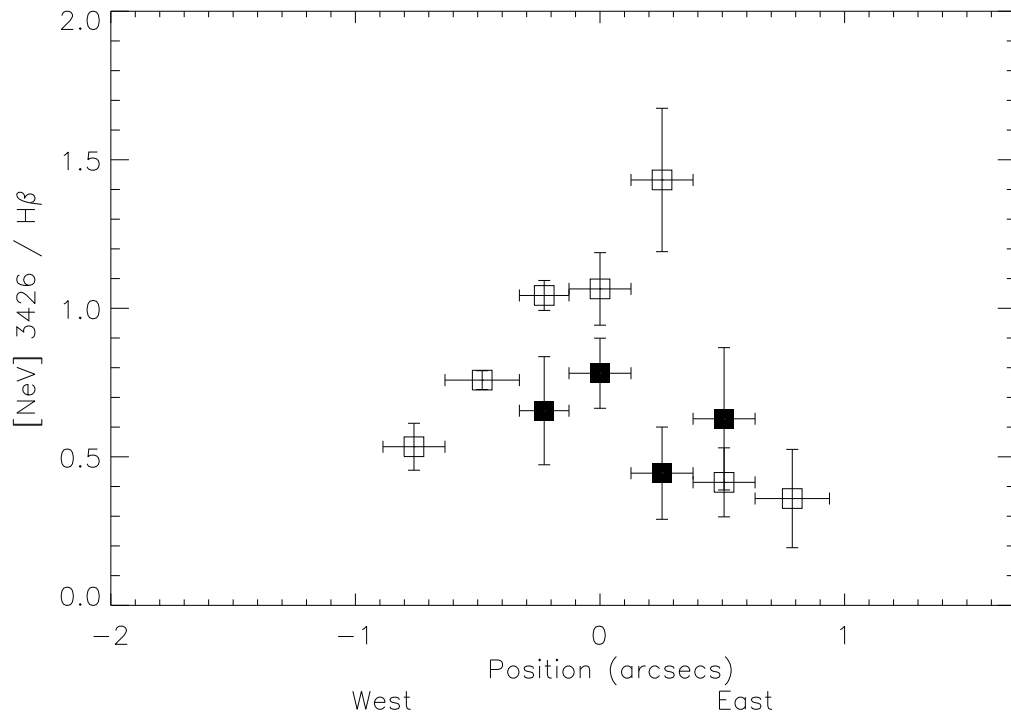


Fig. 15.— $[\text{Ne V}] \lambda 3426 / \text{H}\beta \lambda 4861$ plotted as a function of angular separation from the nucleus along the slit. Note the step drop in the ratio to the east.

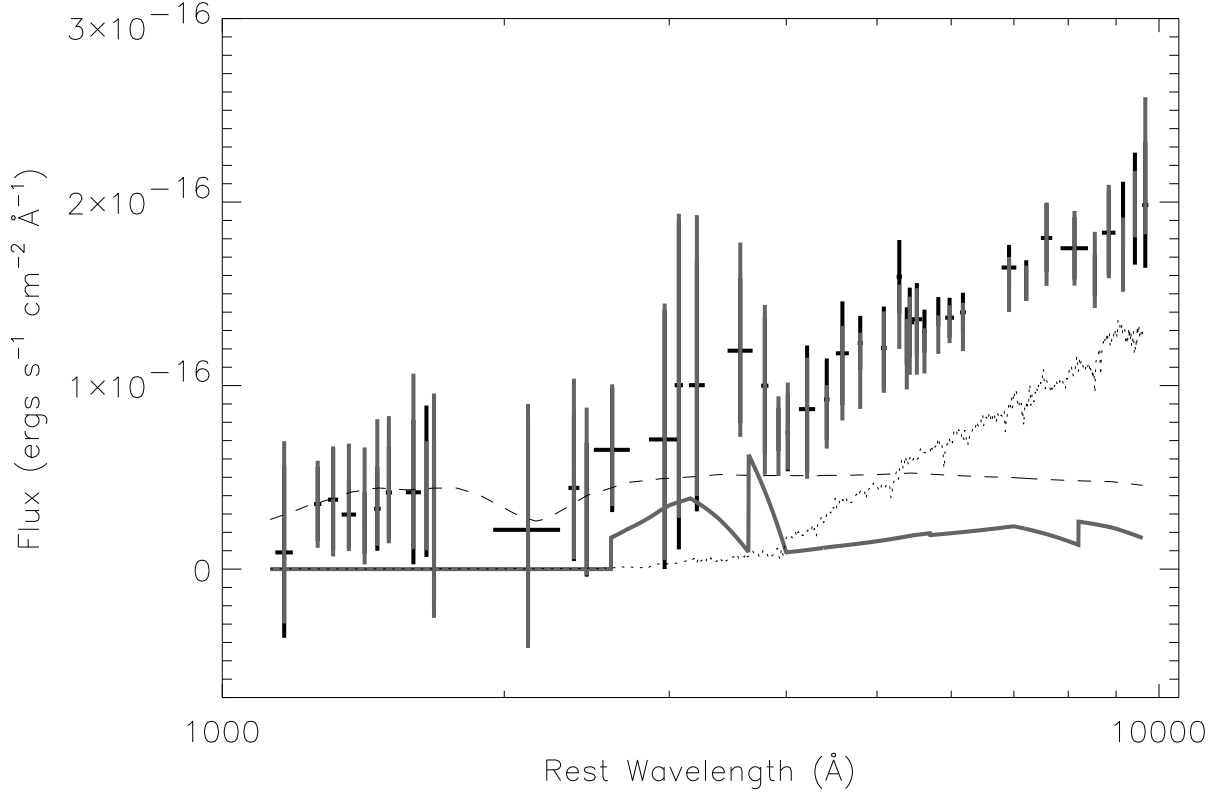


Fig. 16.— The eastern and western extracted continuous spectra (crosses) and individual model components. Crosses denote average continuum values measured between emission lines: the horizontal bar is the width of the measurement region in wavelength, and the vertical bar is the $\pm 1\sigma$ uncertainty in the computed average. Eastern and western extractions are overplotted to emphasize their similarity after accounting for extinction and intrinsic luminosity. The gray crosses represent the eastern extraction corresponding to the region encompassed by bins $+0'.80$ to $+0'.30$ in Figures 8-15. The black crosses represent the western extraction ($+0'.00$ to $-1'.00$) transformed to match the eastern extraction using (1) reddening that corresponds to $E(B-V)=0.08$ with the Koornneef & Code (1981) LMC extinction curve and (2) a multiplicative scale factor of 1.4. The dashed line is the power-law continuum ($\alpha=1$) reddened by an amount corresponding to $E(B-V)=0.08$ with the Koornneef & Code (1981) LMC extinction curve and $E(B-V)=0.19$ with the Galactic extinction curve of Savage & Mathis (1979). The dotted line represents the S0 galaxy template of Kinney et al. (1996) reddened by $E(B-V)=0.28$ with the Koornneef & Code (1981) LMC extinction curve and by $E(B-V)=0.19$ with the Galactic curve (Savage & Mathis 1979). The solid gray line is the NLR gas recombination spectrum reddened in the same manner as the S0 template spectrum. The power-law and S0 galaxy template spectra were scaled so that $f_{galaxy}=0.75$ at 8125\AA and also so that the sum of these components with the recombination spectrum matches the data. A logarithmic wavelength scale, adjusted to the rest-frame of Markarian 3 is used to separate the ultraviolet measurements.

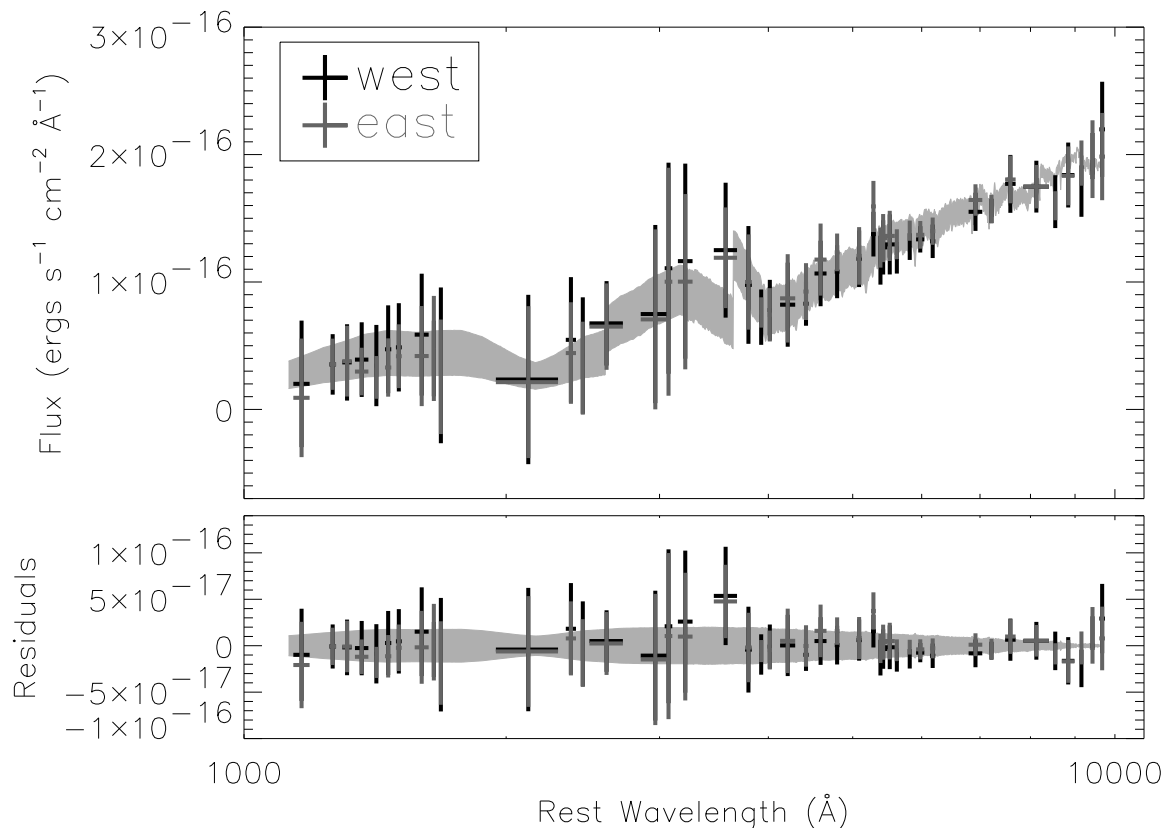


Fig. 17.— The eastern and western extracted continuous spectra (crosses) and the best fit model (thick gray line). The extracted spectra are identical to those shown in Figure 16. The thick gray line shows the variation in the reddened model spectrum (S0 galaxy + power-law + H^+ and He^{+2} recombination continua, see text and Figure 16 caption) when the galaxy fraction ($f_{galaxy} = L_{galaxy}/(L_{galaxy}+L_{scattered-AGN})$) is varied between 0.65 and 0.85 at 8125 Å.

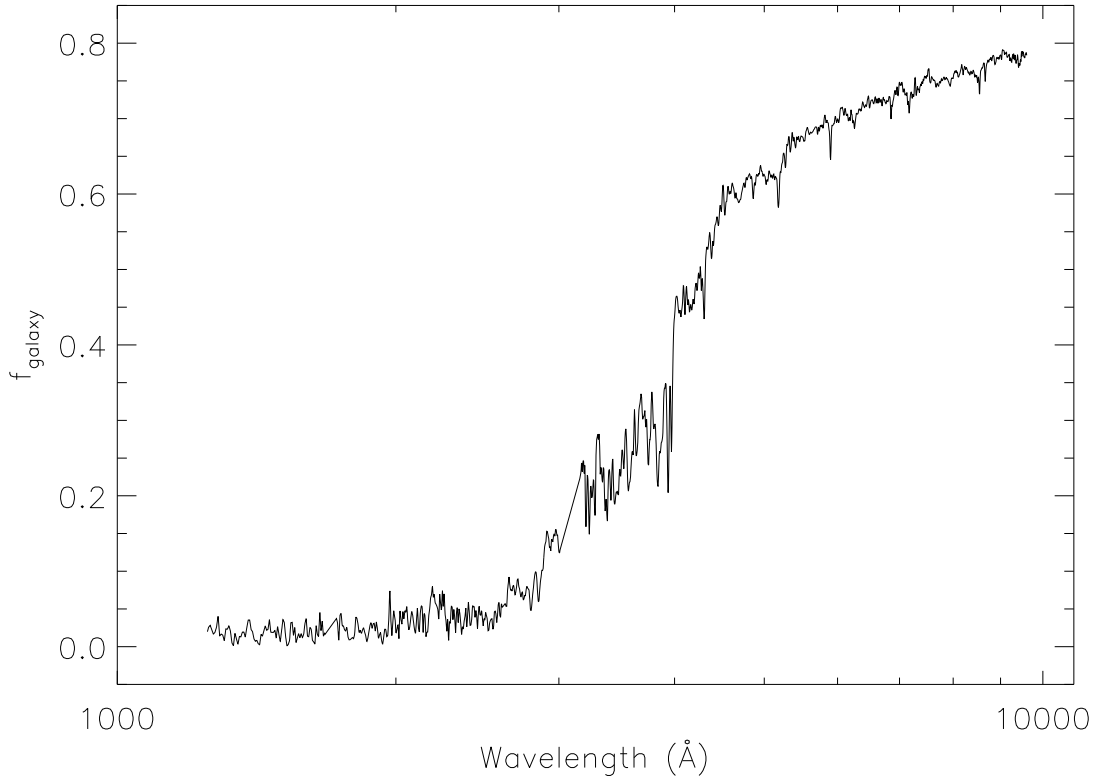


Fig. 18.— The galaxy fraction (f_{galaxy}), or the ratio of host galaxy continuum (Kinney et al. (1996) S0 template) to the sum of the host galaxy continuum and power-law continuum ($\alpha=1$) as a function of wavelength for the best fit to the observed continuum. $f_{galaxy} = L_{galaxy} / (L_{galaxy} + L_{scattered-AGN}) = 0.75$ at 8125 Å.

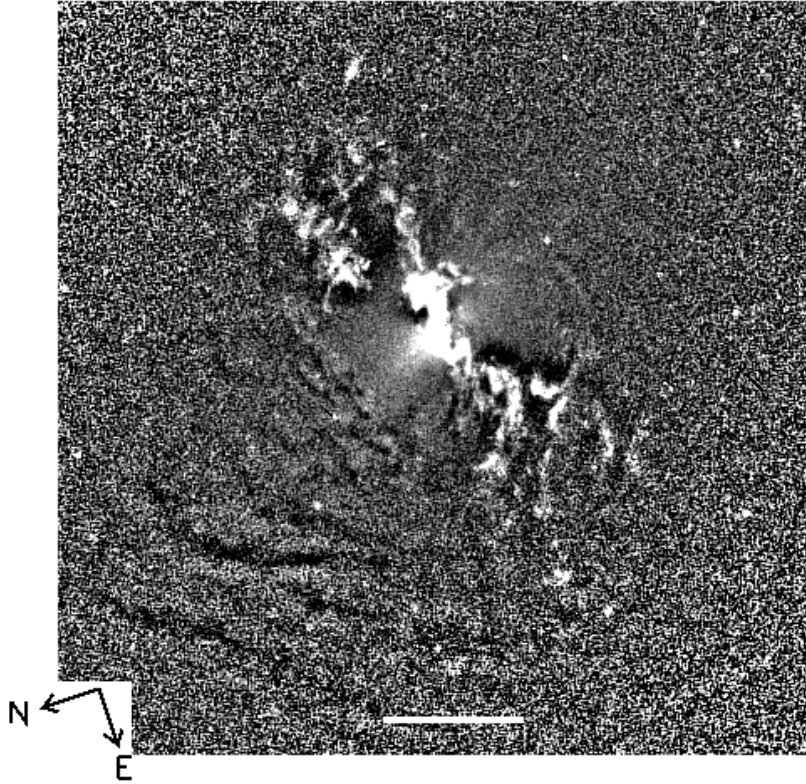


Fig. 19.— Unsharp-masked version of archival HST/WFPC2/F606W image. The unsharp-mask filter size is $1''.43$. The horizontal bar corresponds to $3''.8$ or 1 kpc. The display scaling is such that emitting-material appears white and obscuring materials (i.e., dust lanes) appear black. Note the presence of dust lanes towards the north-east of the NLR and lack of dust lanes to the south-west. The emission in the central region is primarily due to emission-lines from the NLR within the F606W bandpass.

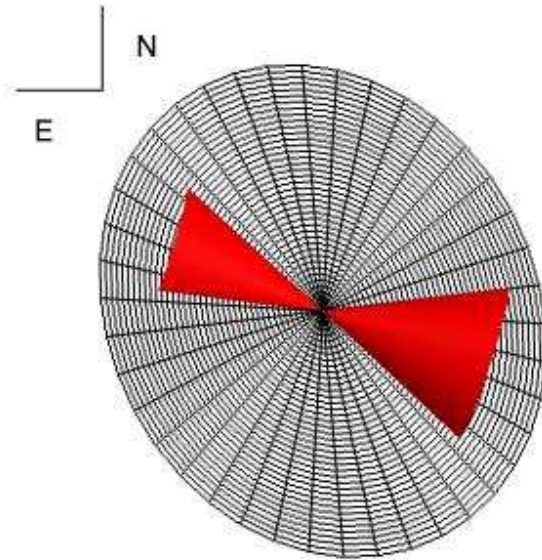


Fig. 20.— Schematic of the Markarian 3 NLR and its relative orientation to the host galaxy disk from the observer’s point-of-view. North is up and East is to the left.

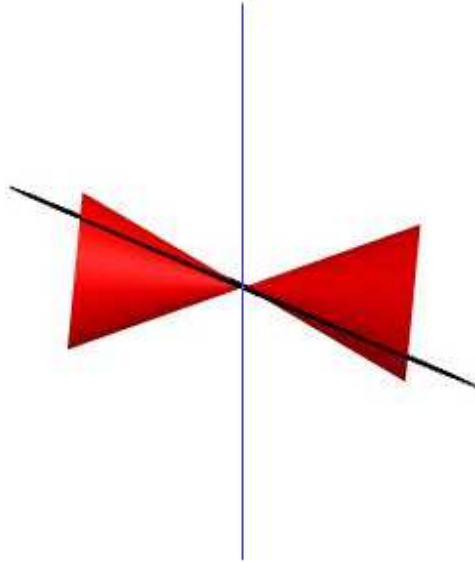


Fig. 21.— Schematic of the Markarian 3 NLR and its relative orientation to the host galaxy disk, which is edge-on in this figure. The projected line-of-sight is from the top of the figure and parallel to the vertical bar. East is to the left of the figure.

Table 1. STIS Long Slit Observations of Markarian 3^a

Data Set Set	Detector	Optical Element	Central Wavelength (Å)	Dispersion Scale (Å/pix)	Spectral Resolution ^b (Å)	Plate Scale ("/pix.)	Aperture (")	Exposure Time (seconds)
(1)	(2)	(3)	(4)	(5)	(6)	(7)	(8)	(9)
O5KS01J6Q	CCD	MIRVIS	7229	N/A	N/A	0.050	F28X50LP	3 ^c
O5KS01010	CCD	G430L	4300	2.73	4.00	0.050	52X0.1	1080
O5KS01020	CCD	G750L	7751	4.92	9.89	0.050	52X0.1	1080
O5KS01040	FUV-MAMA	G140L	1425	0.60	1.13	0.025	52X0.1	3238
O5KS01050	FUV-MAMA	G140L	1425	0.60	1.13	0.025	52X0.1	3238
O5KS01060	NUV-MAMA	G230L	2376	1.58	2.35	0.025	52X0.1	3238

^aObservations were obtained under HST proposal identification number 8480 by Kraemer and Crenshaw.

^bSpectral resolution is full-width at half-maximum (FWHM) in Å and is related to σ (for a Gaussian distribution) by $\sigma = \text{FWHM} / 2.354$.

^cExposure time listed for O5K5S01J6Q is that for the third exposure in the data set. The same exposure is shown in Figure 1.

Table 2. Observed Emission-line Fluxes Relative to $H\beta$

		West						East				
		-0.8 ^a	-0.5	-0.2	-0.2	0.0	0.0	0.3	0.3	0.5	0.5	0.8
		r ^b	r	r	b	r	b	r	b	r	b	r
		0.3 ^c	0.3	0.2	0.2	0.3	0.3	0.3	0.3	0.3	0.3	0.3
(1)	(2)	(3)	(4)	(5)	(6)	(7)	(8)	(9)	(10)	(11)	(12)	(13)
Ly α	1216	4.89 (0.16) ^d	2.01 (0.04)	1.73 (0.02)	1.22 (0.05)	1.52 (0.05)	0.85 (0.03)	0.50 (0.07)	0.30 (0.05)	0.78 (0.05)	0.32 (0.02)	0.78 (0.02)
NV	1240	0.11 (0.01)	0.10 (0.04)	0.09 (0.00)	0.05 (0.01)	0.07 (0.00)	0.03 (0.00)	0.03 (0.00)	0.02 (0.00)	0.01 (0.00)	< 0.02 ^e (0.00)	0.01 (0.01)
CII	1335	0.07 (0.01)	0.02 (0.01)	0.01 (0.00)	0.02 (0.00)	< 0.02 (0.00)	< 0.02 (0.00)	< 0.06 (0.00)	0.00 (0.00)	0.00 (0.00)	0.00 (0.00)	0.02 (0.03)
NIV]	1486	0.06 (0.07)	0.07 (0.00)	0.04 (0.00)	0.10 (0.00)	0.02 (0.00)	0.04 (0.00)	< 0.02 (0.00)	0.02 (0.00)	< 0.01 (0.00)	0.01 (0.00) (.....)
CIV	1548	0.75 (0.02)	0.62 (0.04)	0.81 (0.04)	0.31 (0.01)	0.49 (0.01)	0.22 (0.02)	0.15 (0.02)	0.03 (0.01)	0.14 (0.01)	0.03 (0.02)	0.07 (0.00)
CIV	1551	0.37 (0.01)	0.31 (0.02)	0.41 (0.02)	0.15 (0.00)	0.25 (0.01)	0.11 (0.01)	0.07 (0.01)	0.01 (0.01)	0.07 (0.00)	0.02 (0.01)	0.04 (0.00)
HeII	1640	0.41 (0.02)	0.35 (0.01)	0.38 (0.00)	0.20 (0.01)	0.22 (0.01)	0.19 (0.00)	0.10 (0.01)	0.12 (0.02)	0.13 (0.01)	0.12 (0.01)	0.14 (0.00)
OIII]	1665	0.23 (0.02)	0.04 (0.01)	0.01 (0.01)	0.02 (0.02)	0.01 (0.01)	0.10 (0.01) (.....)	0.01 (0.00)	< 0.01 (0.00)	0.07 (0.00)	0.03 (0.00)
CIII]	1909	1.16 (1.62)	0.46 (0.02)	0.37 (0.00)	0.51 (0.01)	0.09 (0.01)	0.04 (0.00)	0.29 (0.04)	0.10 (0.03)	0.10 (0.01)	0.20 (0.03)	0.31 (0.07)
CII]	2324	0.44 (0.55)	0.15 (0.00)	0.13 (0.00)	0.16 (0.00)	0.11 (0.00)	0.11 (0.00)	0.09 (0.02)	0.10 (0.01)	0.13 (0.01)	0.10 (0.01)	0.21 (0.01)
[NeIV]	2424	0.25 (0.04)	0.24 (0.02)	0.26 (0.00)	0.15 (0.01)	0.18 (0.01)	0.10 (0.01)	0.14 (0.02)	0.05 (0.01)	0.08 (0.01)	0.06 (0.00)	0.03 (0.02)
[OII]	2470 (.....)	0.09 (0.00)	0.05 (0.00)	0.03 (0.01)	0.02 (0.00)	0.05 (0.01)	0.07 (0.01)	< 0.03 (0.00)	0.05 (0.00)	0.04 (0.00)	0.08 (0.01)

Table 2—Continued

		West						East				
		-0.8 ^a	-0.5	-0.2	-0.2	0.0	0.0	0.3	0.3	0.5	0.5	0.8
		r ^b	r	r	b	r	b	r	b	r	b	r
		0.3 ^c	0.3	0.2	0.2	0.3	0.3	0.3	0.3	0.3	0.3	0.3
(1)	(2)	(3)	(4)	(5)	(6)	(7)	(8)	(9)	(10)	(11)	(12)	(13)
MgII	2796	0.62 (0.02)	0.28 (0.01)	0.14 (0.01)	0.32 (0.04)	0.27 (0.01)	0.19 (0.01)	0.11 (0.02)	0.10 (0.01)	0.23 (0.02)	0.17 (0.02)	0.21 (0.04)
MgII	2803	0.31 (0.01)	0.14 (0.01)	0.07 (0.01)	0.16 (0.02)	0.14 (0.01)	0.09 (0.01)	0.06 (0.01)	0.05 (0.01)	0.12 (0.01)	0.08 (0.01)	0.10 (0.02)
[OIII]	3133	0.17 (0.20)	0.13 (0.01)	0.21 (0.00)	0.10 (0.00)	0.17 (0.01)	0.05 (0.02)	0.21 (0.03)	0.06 (0.02)	0.09 (0.01)	0.16 (0.01)	< 3.13 (0.00)
[NeV]	3346	0.12 (0.10)	0.15 (0.01)	0.25 (0.00)	0.11 (0.01)	0.24 (0.01)	0.17 (0.02)	0.18 (0.03)	0.16 (0.02)	0.10 (0.01)	0.02 (0.01)	0.18 (0.28)
[NeV]	3426	0.35 (0.01)	0.49 (0.01)	0.65 (0.01)	0.41 (0.01)	0.61 (0.02)	0.44 (0.02)	0.61 (0.08)	0.25 (0.04)	0.23 (0.02)	0.33 (0.02)	0.18 (0.00)
[OII]	3727	2.94 (0.09)	1.22 (0.02)	1.13 (0.01)	1.45 (0.03)	1.59 (0.05)	1.66 (0.04)	0.71 (0.19)	1.54 (0.18)	1.89 (0.12)	1.57 (0.08)	1.73 (0.03)
[NeIII]	3869	1.03 (0.03)	1.06 (0.05)	1.07 (0.01)	0.86 (0.02)	0.95 (0.03)	0.94 (0.03)	0.97 (0.14)	0.67 (0.11)	0.86 (0.05)	0.82 (0.04)	0.80 (0.02)
H8	3889	0.11 (0.01)	0.12 (0.02)	0.12 (0.00)	0.10 (0.01)	0.24 (0.23)	0.07 (0.03)	0.14 (0.02)	0.09 (0.03)	0.10 (0.01)	< 0.02 (0.00)	0.10 (0.02)
[NeIII]	3968	0.46 (0.04)	0.41 (0.02)	0.40 (0.01)	0.32 (0.03)	0.37 (0.03)	0.27 (0.03)	0.38 (0.05)	0.22 (0.04)	0.36 (0.03)	0.25 (0.03)	0.35 (0.02)
[SII]	4074	0.06 (0.03)	0.16 (0.01)	0.15 (0.01)	0.07 (0.02)	0.20 (0.02)	0.12 (0.03)	0.23 (0.03)	0.13 (0.03)	0.35 (0.03)	0.27 (0.03)	0.33 (0.02)
H δ	4102	0.15 (0.04)	0.15 (0.01)	0.17 (0.01)	0.13 (0.02)	0.14 (0.02)	0.17 (0.02)	0.16 (0.02)	0.11 (0.03)	0.12 (0.02)	0.13 (0.02)	0.15 (0.02)
H γ	4340	0.30 (0.03)	0.35 (0.02)	0.35 (0.01)	0.29 (0.04)	0.36 (0.02)	0.34 (0.03)	0.37 (0.05)	0.29 (0.05)	0.39 (0.03)	0.32 (0.03)	0.34 (0.01)

Table 2—Continued

		West						East				
		-0.8 ^a	-0.5	-0.2	-0.2	0.0	0.0	0.3	0.3	0.5	0.5	0.8
		r ^b	r	r	b	r	b	r	b	r	b	r
(1)	(2)	0.3 ^c	0.3	0.2	0.2	0.3	0.3	0.3	0.3	0.3	0.3	0.3
(1)	(2)	(3)	(4)	(5)	(6)	(7)	(8)	(9)	(10)	(11)	(12)	(13)
[OIII]	4363	0.16	0.18	0.17	0.22	0.18	0.24	0.25	0.16	0.14	0.13	0.17
		(0.03)	(0.02)	(0.01)	(0.03)	(0.02)	(0.02)	(0.03)	(0.03)	(0.02)	(0.01)	(0.01)
HeII	4686	0.24	0.23	0.28	0.14	0.22	0.20	0.30	0.13	0.15	0.15	0.25
		(0.01)	(0.00)	(0.01)	(0.01)	(0.01)	(0.01)	(0.04)	(0.01)	(0.01)	(0.01)	(0.05)
H β	4861	1.00	1.00	1.00	1.00	1.00	1.00	1.00	1.00	1.00	1.00	1.00
		(0.03)	(0.02)	(0.01)	(0.02)	(0.04)	(0.02)	(0.17)	(0.12)	(0.09)	(0.05)	(0.02)
[OIII]	4959	4.15	4.93	5.35	4.57	4.78	5.11	5.59	3.83	3.97	3.80	3.55
		(0.23)	(0.63)	(0.04)	(0.08)	(0.16)	(0.12)	(0.86)	(0.56)	(0.25)	(0.20)	(0.10)
[OIII]	5007	12.73	14.95	16.37	14.02	14.90	14.55	17.05	11.63	11.77	11.97	10.37
		(0.32)	(0.45)	(0.12)	(0.25)	(0.62)	(0.51)	(2.39)	(1.55)	(0.73)	(0.64)	(0.25)
[FeVII]	5159	0.14	0.03	0.04	0.12	0.04	0.09	0.03	0.08	0.09	0.08	0.11
		(0.02)	(0.01)	(0.01)	(0.03)	(0.01)	(0.02)	(0.01)	(0.02)	(0.01)	(0.02)	(0.01)
[NI]	5200	0.16	0.07	0.08	0.10	0.10	0.22	0.09	0.20	0.21	0.26	0.21
		(0.02)	(0.01)	(0.01)	(0.02)	(0.01)	(0.01)	(0.03)	(0.02)	(0.02)	(0.02)	(0.01)
[FeVII]	5722	0.17	0.08	0.10	< 0.03	0.12	0.05	0.08	0.09	0.02	< 0.04	0.03
		(0.02)	(0.01)	(0.00)	(0.00)	(0.01)	(0.02)	(0.01)	(0.01)	(0.00)	(0.00)	(0.00)
[NII]	5755	0.15	0.09	0.05	0.11	0.07	0.13	0.10	0.09	0.11	0.16	0.12
		(0.02)	(0.01)	(0.00)	(0.01)	(0.01)	(0.01)	(0.02)	(0.01)	(0.01)	(0.01)	(0.00)
HeI	5876	0.23	0.11	0.11	0.14	0.07	0.16	0.07	0.16	0.12	0.18	0.17
		(0.03)	(0.01)	(0.00)	(0.00)	(0.01)	(0.01)	(0.02)	(0.03)	(0.01)	(0.01)	(0.00)
[FeVII]	6087	0.11	0.13	< 0.15	0.16	0.15	0.16	0.11	0.06	0.04	0.05
		(.....)	(0.01)	(0.01)	(0.00)	(0.02)	(0.02)	(0.02)	(0.03)	(0.01)	(0.02)	(0.01)
[OI]	6300	1.02	0.69	0.77	0.86	1.04	1.40	1.50	1.32	1.89	1.73	1.45
		(0.03)	(0.02)	(0.01)	(0.02)	(0.03)	(0.06)	(0.24)	(0.16)	(0.12)	(0.08)	(0.03)

Table 2—Continued

(1)	(2)	West						East				
		-0.8 ^a	-0.5	-0.2	-0.2	0.0	0.0	0.3	0.3	0.5	0.5	0.8
		r ^b	r	r	b	r	b	r	b	r	b	r
		0.3 ^c	0.3	0.2	0.2	0.3	0.3	0.3	0.3	0.3	0.3	0.3
(3)	(4)	(5)	(6)	(7)	(8)	(9)	(10)	(11)	(12)	(13)		
[OI]	6363	0.47 (0.02)	0.22 (0.01)	0.25 (0.00)	0.30 (0.02)	0.38 (0.02)	0.47 (0.03)	0.54 (0.09)	0.42 (0.05)	0.58 (0.04)	0.69 (0.04)	0.49 (0.01)
[NII]	6548	1.98 (0.08)	1.27 (0.10)	1.17 (0.01)	2.25 (0.14)	1.62 (0.05)	2.59 (0.04)	1.94 (0.34)	2.21 (0.38)	2.64 (0.20)	2.66 (0.22)	2.10 (0.05)
H α	6563	4.84 (0.14)	4.37 (0.10)	3.29 (0.26)	3.74 (0.22)	3.75 (0.18)	5.61 (0.21)	6.08 (1.18)	4.25 (0.90)	5.11 (0.55)	5.10 (0.40)	4.31 (0.25)
[NII]	6584	5.89 (0.19)	3.65 (0.13)	3.51 (0.03)	6.77 (0.43)	4.93 (0.16)	7.78 (0.12)	5.85 (0.80)	5.80 (0.86)	7.96 (0.60)	8.40 (0.52)	6.34 (0.16)
HeI	7065	< 0.05 (0.00)	0.05 (0.00)	0.08 (0.01)	0.05 (0.02)	0.15 (0.01)	0.18 (0.01)	0.13 (0.02)	0.10 (0.01)	0.10 (0.01)	0.04 (0.01)	0.05 (0.01)
[ArIII]	7135	0.23 (0.04)	0.36 (0.01)	0.36 (0.01)	0.33 (0.02)	0.42 (0.01)	0.46 (0.01)	0.56 (0.08)	0.26 (0.04)	0.62 (0.04)	0.32 (0.02)	0.41 (0.01)
[OII]	7325	0.32 (0.15)	0.46 (0.02)	0.43 (0.00)	0.31 (0.01)	0.67 (0.02)	0.40 (0.01)	0.83 (0.12)	0.42 (0.06)	1.17 (0.07)	0.70 (0.04)	0.86 (0.06)
[ArIII]	7751	0.30 (0.02)	0.16 (0.02)	0.13 (0.00)	0.11 (0.00)	0.16 (0.01)	0.07 (0.01)	0.16 (0.02)	0.08 (0.01)	0.17 (0.01)	0.02 (0.01)	0.08 (0.01)
[SIII]	9069	1.42 (0.04)	1.21 (0.06)	1.26 (0.01)	1.12 (0.02)	1.57 (0.04)	1.79 (0.03)	2.12 (0.30)	1.10 (0.18)	1.83 (0.11)	1.37 (0.07)	1.25 (0.12)
[SIII]	9532	2.42 (0.08)	2.41 (0.05)	2.55 (0.03)	2.25 (0.07)	4.21 (0.11)	3.47 (0.06)	5.01 (0.68)	2.58 (0.44)	5.17 (0.32)	2.60 (0.14)	3.44 (0.08)
f _{Hβ} ^f	4861	1.62 (0.04)	10.12 (0.14)	6.52 (0.05)	2.89 (0.05)	3.72 (0.09)	2.96 (0.04)	4.69 (0.56)	4.69 (0.40)	6.91 (0.42)	3.73 (0.14)	7.09 (0.10)

^aProjected angular distance from nucleus in arcseconds.

^bMeasurement is blue-shifted (b) or red-shifted(r) with respect to the Markarian 3 rest-frame.

^cAngular width of measurement bin in arcseconds.

^dThe 1σ measurement uncertainty is listed in parenthesis below each measurement

^e< indicates that the recorded value is the 1σ upper limit.

^f $H\beta$ fluxes are in units of 10^{-15} ergs sec⁻¹ cm⁻².

Table 3. Extinction Corrected Emission-line Fluxes Relative to $H\beta$

		West						East				
		-0.8 ^a	-0.5	-0.2	-0.2	0.0	0.0	0.3	0.3	0.5	0.5	0.8
		r ^b	r	r	b	r	b	r	b	r	b	r
		0.3 ^c	0.3	0.2	0.2	0.3	0.3	0.3	0.3	0.3	0.3	0.3
(1)	(2)	(3)	(4)	(5)	(6)	(7)	(8)	(9)	(10)	(11)	(12)	(13)
E(B-V)		0.12 (0.02) ^d	0.14 (0.01)	0.16 (0.01)	0.15 (0.05)	0.21 (0.02)	0.22 (0.02)	0.40 (0.02)	0.22 (0.05)	0.24 (0.04)	0.26 (0.06)	0.31 (0.08)
Ly α	1216	42.54 (13.18)	20.81 (1.48)	21.30 (2.18)	14.08 (8.35)	29.68 (7.08)	18.58 (5.76)	54.35 (14.72)	6.78 (4.69)	19.97 (11.55)	9.90 (7.97)	38.97 (38.35)
NV	1240	0.86 (0.28)	0.98 (0.42)	1.05 (0.11)	0.49 (0.32)	1.29 (0.31)	0.69 (0.22)	2.46 (0.66)	0.40 (0.28)	0.22 (0.13)	< 0.46 ^e (0.00)	0.56 (0.84)
CII	1335	0.42 (0.14)	0.13 (0.09)	0.05 (0.01)	0.16 (0.09)	< 0.22 (0.00)	< 0.32 (0.00)	< 3.27 (0.00)	0.02 (0.03)	0.06 (0.04)	0.06 (0.07)	0.69 (1.17)
NIV]	1486	0.31 (0.35)	0.37 (0.03)	0.25 (0.02)	0.59 (0.29)	0.15 (0.04)	0.41 (0.12)	< 0.59 (0.00)	0.20 (0.11)	< 0.15 (0.00)	0.15 (0.10) (.....)
CIV	1548	3.54 (0.89)	3.36 (0.27)	4.95 (0.47)	1.79 (0.86)	4.19 (0.81)	2.04 (0.54)	4.35 (1.00)	0.27 (0.19)	1.42 (0.67)	0.38 (0.31)	1.21 (0.97)
CIV	1551	1.77 (0.44)	1.68 (0.14)	2.47 (0.23)	0.89 (0.43)	2.09 (0.40)	1.02 (0.27)	2.16 (0.50)	0.14 (0.10)	0.70 (0.33)	0.19 (0.15)	0.60 (0.48)
HeII	1640	1.80 (0.44)	1.73 (0.10)	2.09 (0.17)	1.07 (0.49)	1.65 (0.31)	1.51 (0.36)	2.32 (0.52)	0.97 (0.52)	1.19 (0.55)	1.17 (0.75)	1.94 (1.49)
OIII]	1665	0.97 (0.24)	0.21 (0.05)	0.05 (0.03)	0.12 (0.12)	0.09 (0.04)	0.82 (0.20) (.....)	0.11 (0.07)	< 0.05 (0.00)	0.67 (0.42)	0.45 (0.35)
CIII]	1909	4.74 (6.71)	2.09 (0.14)	1.85 (0.13)	2.45 (1.03)	0.58 (0.13)	0.24 (0.05)	4.99 (1.07)	0.71 (0.39)	0.77 (0.32)	1.65 (0.97)	3.43 (2.54)
CII]	2324	1.66 (2.11)	0.62 (0.03)	0.57 (0.04)	0.69 (0.26)	0.59 (0.09)	0.64 (0.13)	1.13 (0.26)	0.60 (0.27)	0.81 (0.31)	0.68 (0.36)	1.84 (1.17)
[NeIV]	2424	0.76 (0.19)	0.78 (0.08)	0.91 (0.06)	0.50 (0.18)	0.76 (0.11)	0.46 (0.09)	1.17 (0.22)	0.22 (0.09)	0.38 (0.13)	0.31 (0.15)	0.16 (0.14)

Table 3—Continued

		West						East				
		-0.8 ^a	-0.5	-0.2	-0.2	0.0	0.0	0.3	0.3	0.5	0.5	0.8
		r ^b	r	r	b	r	b	r	b	r	b	r
		0.3 ^c	0.3	0.2	0.2	0.3	0.3	0.3	0.3	0.3	0.3	0.3
(1)	(2)	(3)	(4)	(5)	(6)	(7)	(8)	(9)	(10)	(11)	(12)	(13)
[OII]	2470	0.26	0.16	0.09	0.07	0.21	0.47	< 0.11	0.22	0.17	0.40
		(.....)	(0.01)	(0.01)	(0.04)	(0.02)	(0.04)	(0.09)	(0.00)	(0.08)	(0.08)	(0.23)
MgII	2796	1.27	0.60	0.32	0.71	0.70	0.50	0.47	0.26	0.64	0.49	0.69
		(0.21)	(0.04)	(0.03)	(0.24)	(0.09)	(0.09)	(0.11)	(0.10)	(0.20)	(0.22)	(0.37)
MgII	2803	0.64	0.30	0.16	0.36	0.35	0.25	0.23	0.13	0.32	0.24	0.34
		(0.10)	(0.02)	(0.02)	(0.12)	(0.05)	(0.04)	(0.05)	(0.05)	(0.10)	(0.11)	(0.19)
[OIII]	3133	0.29	0.24	0.39	0.19	0.34	0.11	0.63	0.13	0.19	0.35	< 7.43
		(0.34)	(0.01)	(0.02)	(0.05)	(0.04)	(0.04)	(0.11)	(0.05)	(0.06)	(0.14)	(0.00)
[NeV]	3346	0.19	0.24	0.41	0.18	0.43	0.31	0.44	0.30	0.19	0.03	0.38
		(0.15)	(0.02)	(0.02)	(0.05)	(0.05)	(0.06)	(0.08)	(0.10)	(0.06)	(0.03)	(0.62)
[NeV]	3426	0.53	0.76	1.04	0.66	1.07	0.78	1.43	0.44	0.41	0.63	0.36
		(0.08)	(0.03)	(0.05)	(0.18)	(0.12)	(0.12)	(0.24)	(0.16)	(0.12)	(0.24)	(0.17)
[OII]	3727	4.05	1.72	1.64	2.08	2.45	2.60	1.39	2.44	3.03	2.58	3.05
		(0.57)	(0.06)	(0.08)	(0.55)	(0.27)	(0.36)	(0.40)	(0.78)	(0.80)	(0.93)	(1.34)
[NeIII]	3869	1.36	1.43	1.47	1.17	1.38	1.38	1.72	0.99	1.29	1.26	1.30
		(0.19)	(0.08)	(0.07)	(0.30)	(0.15)	(0.19)	(0.30)	(0.33)	(0.33)	(0.44)	(0.56)
H8	3889	0.14	0.16	0.17	0.14	0.35	0.11	0.24	0.13	0.15	< 0.02	0.17
		(0.02)	(0.03)	(0.01)	(0.04)	(0.34)	(0.04)	(0.04)	(0.05)	(0.04)	(0.00)	(0.08)
[NeIII]	3968	0.59	0.53	0.53	0.42	0.52	0.38	0.63	0.32	0.52	0.37	0.54
		(0.09)	(0.03)	(0.03)	(0.11)	(0.06)	(0.07)	(0.10)	(0.11)	(0.13)	(0.13)	(0.23)
[SII]	4074	0.07	0.20	0.19	0.10	0.27	0.17	0.36	0.17	0.48	0.37	0.48
		(0.04)	(0.02)	(0.01)	(0.03)	(0.04)	(0.04)	(0.06)	(0.07)	(0.12)	(0.13)	(0.20)
H δ	4102	0.18	0.19	0.21	0.17	0.18	0.22	0.25	0.15	0.16	0.18	0.21
		(0.05)	(0.02)	(0.01)	(0.05)	(0.03)	(0.04)	(0.04)	(0.06)	(0.05)	(0.07)	(0.09)

Table 3—Continued

		West						East				
		-0.8 ^a	-0.5	-0.2	-0.2	0.0	0.0	0.3	0.3	0.5	0.5	0.8
		r ^b	r	r	b	r	b	r	b	r	b	r
(1)	(2)	0.3 ^c	0.3	0.2	0.2	0.3	0.3	0.3	0.3	0.3	0.3	0.3
(1)	(2)	(3)	(4)	(5)	(6)	(7)	(8)	(9)	(10)	(11)	(12)	(13)
H γ	4340	0.34 (0.06)	0.40 (0.03)	0.41 (0.02)	0.34 (0.09)	0.43 (0.04)	0.41 (0.06)	0.49 (0.08)	0.34 (0.11)	0.47 (0.11)	0.39 (0.13)	0.43 (0.17)
[OIII]	4363	0.18 (0.04)	0.20 (0.02)	0.20 (0.02)	0.26 (0.07)	0.21 (0.03)	0.29 (0.04)	0.32 (0.05)	0.20 (0.06)	0.17 (0.04)	0.15 (0.05)	0.21 (0.08)
HeII	4686	0.25 (0.03)	0.24 (0.01)	0.29 (0.01)	0.15 (0.04)	0.23 (0.02)	0.21 (0.03)	0.32 (0.05)	0.13 (0.04)	0.17 (0.04)	0.16 (0.05)	0.27 (0.11)
H β	4861	1.00 (0.12)	1.00 (0.03)	1.00 (0.04)	1.00 (0.22)	1.00 (0.09)	1.00 (0.12)	1.00 (0.19)	1.00 (0.28)	1.00 (0.23)	1.00 (0.30)	1.00 (0.37)
[OIII]	4959	4.04 (0.51)	4.80 (0.63)	5.20 (0.20)	4.44 (0.96)	4.63 (0.43)	4.94 (0.57)	5.33 (0.94)	3.71 (1.06)	3.84 (0.84)	3.66 (1.09)	3.41 (1.23)
[OIII]	5007	12.26 (1.41)	14.37 (0.56)	15.69 (0.59)	13.45 (2.90)	14.20 (1.35)	13.84 (1.63)	15.87 (2.61)	11.06 (3.07)	11.17 (2.44)	11.34 (3.37)	9.75 (3.50)
[FeVII]	5159	0.13 (0.02)	0.03 (0.01)	0.04 (0.01)	0.11 (0.04)	0.03 (0.01)	0.08 (0.02)	0.03 (0.01)	0.08 (0.02)	0.08 (0.02)	0.07 (0.02)	0.09 (0.03)
[NI]	5200	0.15 (0.02)	0.07 (0.01)	0.07 (0.01)	0.10 (0.03)	0.09 (0.01)	0.19 (0.02)	0.08 (0.02)	0.17 (0.05)	0.19 (0.04)	0.23 (0.07)	0.18 (0.06)
[FeVII]	5722	0.14 (0.02)	0.06 (0.01)	0.08 (0.00)	< 0.02 (0.00)	0.10 (0.01)	0.04 (0.01)	0.05 (0.01)	0.07 (0.02)	0.02 (0.00)	< 0.03 (0.00)	0.02 (0.01)
[NII]	5755	0.12 (0.02)	0.07 (0.01)	0.04 (0.00)	0.09 (0.02)	0.06 (0.01)	0.10 (0.01)	0.07 (0.01)	0.07 (0.02)	0.08 (0.02)	0.12 (0.03)	0.09 (0.03)
HeI	5876	0.19 (0.03)	0.09 (0.01)	0.09 (0.00)	0.11 (0.02)	0.06 (0.01)	0.12 (0.01)	0.05 (0.01)	0.12 (0.03)	0.09 (0.02)	0.13 (0.04)	0.12 (0.04)
[FeVII]	6087 (.....)	0.08 (0.01)	0.10 (0.01)	< 0.12 (0.00)	0.12 (0.01)	0.11 (0.02)	0.10 (0.02)	0.08 (0.03)	0.04 (0.01)	0.03 (0.01)	0.03 (0.01)

Table 3—Continued

(1)	(2)	West						East				
		-0.8 ^a	-0.5	-0.2	-0.2	0.0	0.0	0.3	0.3	0.5	0.5	0.8
		r ^b	r	r	b	r	b	r	b	r	b	r
		0.3 ^c	0.3	0.2	0.2	0.3	0.3	0.3	0.3	0.3	0.3	0.3
(3)	(4)	(5)	(6)	(7)	(8)	(9)	(10)	(11)	(12)	(13)		
[OI]	6300	0.77 (0.08)	0.52 (0.02)	0.57 (0.02)	0.63 (0.12)	0.72 (0.06)	0.96 (0.10)	0.88 (0.16)	0.90 (0.23)	1.28 (0.25)	1.15 (0.31)	0.92 (0.29)
[OI]	6363	0.35 (0.04)	0.16 (0.01)	0.18 (0.01)	0.22 (0.04)	0.26 (0.02)	0.32 (0.04)	0.31 (0.06)	0.29 (0.07)	0.39 (0.08)	0.45 (0.12)	0.30 (0.10)
[NII]	6548	1.45 (0.15)	0.91 (0.08)	0.82 (0.03)	1.58 (0.32)	1.08 (0.09)	1.70 (0.17)	1.06 (0.20)	1.44 (0.39)	1.70 (0.34)	1.68 (0.45)	1.26 (0.40)
H α	6563	3.52 (0.36)	3.12 (0.10)	2.30 (0.20)	2.63 (0.52)	2.48 (0.22)	3.67 (0.38)	3.31 (0.69)	2.77 (0.83)	3.28 (0.70)	3.21 (0.86)	2.56 (0.82)
[NII]	6584	4.27 (0.44)	2.59 (0.11)	2.44 (0.08)	4.75 (0.94)	3.25 (0.27)	5.07 (0.50)	3.16 (0.49)	3.76 (0.98)	5.09 (1.01)	5.26 (1.38)	3.75 (1.18)
HeI	7065	< 0.04 (0.00)	0.03 (0.00)	0.05 (0.00)	0.04 (0.02)	0.09 (0.01)	0.11 (0.01)	0.06 (0.01)	0.06 (0.01)	0.06 (0.01)	0.02 (0.01)	0.03 (0.01)
[ArIII]	7135	0.16 (0.03)	0.24 (0.01)	0.23 (0.01)	0.21 (0.04)	0.25 (0.02)	0.27 (0.03)	0.26 (0.04)	0.15 (0.04)	0.35 (0.07)	0.18 (0.04)	0.22 (0.07)
[OII]	7325	0.21 (0.10)	0.29 (0.01)	0.27 (0.01)	0.20 (0.04)	0.39 (0.03)	0.23 (0.02)	0.37 (0.06)	0.24 (0.06)	0.66 (0.12)	0.38 (0.10)	0.43 (0.13)
[ArIII]	7751	0.19 (0.02)	0.10 (0.01)	0.08 (0.00)	0.07 (0.01)	0.09 (0.01)	0.04 (0.01)	0.06 (0.01)	0.04 (0.01)	0.09 (0.02)	0.01 (0.00)	0.04 (0.01)
[SIII]	9069	0.77 (0.07)	0.63 (0.03)	0.63 (0.02)	0.57 (0.10)	0.71 (0.05)	0.79 (0.07)	0.65 (0.10)	0.48 (0.12)	0.78 (0.14)	0.56 (0.13)	0.46 (0.14)
[SIII]	9532	1.28 (0.12)	1.22 (0.04)	1.24 (0.04)	1.12 (0.19)	1.85 (0.13)	1.48 (0.13)	1.48 (0.22)	1.09 (0.28)	2.13 (0.37)	1.03 (0.24)	1.21 (0.34)
f _{Hβ} ^f	4861	4.55	30.28	20.81	9.03	14.10	11.71	33.79	18.87	28.97	16.77	38.12

Table 3—Continued

		West						East				
		-0.8 ^a	-0.5	-0.2	-0.2	0.0	0.0	0.3	0.3	0.5	0.5	0.8
		r ^b	r	r	b	r	b	r	b	r	b	r
		0.3 ^c	0.3	0.2	0.2	0.3	0.3	0.3	0.3	0.3	0.3	0.3
(1)	(2)	(3)	(4)	(5)	(6)	(7)	(8)	(9)	(10)	(11)	(12)	(13)
		(0.38)	(0.69)	(0.57)	(1.41)	(0.94)	(0.96)	(4.56)	(3.67)	(4.71)	(3.59)	(9.85)

^aProjected angular distance from nucleus in arcseconds.

^bMeasurement is blue-shifted (b) or red-shifted(r) with respect to the Markarian 3 rest-frame.

^cAngular width of measurement bin in arcseconds.

^dThe 1σ measurement uncertainty is listed in parenthesis below each measurement

^e< indicates that the recorded value is the 1σ upper limit.

^fH β fluxes are in units of 10^{-15} ergs sec⁻¹ cm⁻².